Complex critical points and curved geometries in four-dimensional Lorentzian spinfoam quantum gravity

Muxin Han, Zichang Huang, Hongguang Liu, and Dongxue Qu

Phys. Rev. D **106**, 044005 — Published 10 August 2022

DOI: 10.1103/PhysRevD.106.044005

Complex critical points and curved geometries in four-dimensional Lorentzian spinfoam quantum gravity

Muxin Han[1,2] **Zichang Huang**[3,4] **Hongguang Liu**[2] **Dongxue Qu**[1]

[1] *Department of Physics, Florida Atlantic University, 777 Glades Road, Boca Raton, FL 33431-0991, USA*

[2] *Institut für Quantengravitation, Universität Erlangen-Nürnberg, Staudtstr. 7/B2, 91058 Erlangen, Germany*

[3] *Department of Physics, Center for Field Theory and Particle Physics, and Institute for Nano- electronic devices and Quantum computing, Fudan University, Shanghai 200433, China*

[4] *State Key Laboratory of Surface Physics, Fudan University, Shanghai 200433, China*

E-mail: dqu2017@fau.edu

Abstract: This paper focuses on the semiclassical behavior of the spinfoam quantum gravity in 4 dimensions. There has been long-standing confusion, known as the flatness problem, about whether the curved geometry exists in the semiclassical regime of the spinfoam amplitude. The confusion is resolved by the present work. By numerical computations, we explicitly find curved Regge geometries that contribute dominantly to the large-j Lorentzian Engle-Pereira-Rovelli-Livine (EPRL) spinfoam amplitudes on triangulations. These curved geometries are with small deficit angles and relate to the complex critical points of the amplitude. The dominant contribution from the curved geometry to the spinfoam amplitude is proportional to $e^{i\mathcal{I}}$, where $\mathcal{I}$ is the Regge action of the geometry plus corrections of higher order in curvature. As a result, In the semiclassical regime, the spinfoam amplitude reduces to an integral over Regge geometries weighted by $e^{i\mathcal{I}}$, where $\mathcal{I}$ is the Regge action plus corrections of higher order in curvature. As a byproduct, our result also provides a mechanism to relax the cosine problem in the spinfoam model. Our results provide important evidence supporting the semiclassical consistency of the spinfoam quantum gravity.

Contents

1 Introduction

The semiclassical consistency is an important requirement in quantum physics. Any satisfactory quantum theory must reproduce the corresponding classical theory in the approximation of small $\hbar$. In particular, the semiclassical analysis is more crucial in the field of quantum gravity. Due to the limitation of experimental tests, the semiclassical consistency is one of only few physical constraints for quantum gravity: a satisfactory quantum theory of gravity must reproduce General Relativity (GR) in the semiclassical regime.

This paper focuses on the semiclassical analysis of Loop Quantum Gravity (LQG). LQG as a background-independent and non-perturbative approach has been demonstrated to be a competitive candidate toward the final quantum gravity theory (see e.g., [1–6] for reviews). The path integral formulation of LQG, known as the *spinfoam theory* [7–11], is particularly interesting for testing the semiclassical consistency of LQG, because of the connection between the semiclassical approximation of path integral and the stationary phase approximation. A central object in the spinfoam theory is the *spinfoam amplitude*, which defines the covariant transition amplitude of LQG. The recent semiclassical analysis reveals the interesting relation between spinfoam amplitudes and the Regge calculus, which discretizes GR on triangulations [12–19]. This relation makes the semiclassical consistency of the spinfoam theory promising.

Nevertheless, it has been argued that an accidental flatness constraint might emerge in the semiclassical regime so that only flat Regge geometries would dominate spinfoam amplitudes. In contrast, curved geometries were absent [20–24]. The suspicion of lacking curved geometry in the semiclassical regime has led to doubt about the semiclassical behavior. This *flatness problem* has been a key issue in the spinfoam LQG for more than a decade.

In this paper, we resolve the flatness problem by explicitly finding curved Regge geometries from the 4-dimensional Lorentzian EPRL spinfoam amplitude. These curved geometries are with small deficit angles δ_h, and have been overlooked in the model because they correspond to complex critical points slightly away from the real integration domain. But they can be revealed by a more refined stationary phase analysis involving the analytic continuation of the spinfoam integrand. These curved Regge geometries still give non-suppressed dominant contributions to the spinfoam amplitude. The contributions are proportional to $e^{i\mathcal{I}}$ where $\mathcal{I}$ is the Regge action of the curved geometry plus corrections of the second and higher orders in δ_h. The spinfoam amplitude reduces to an integral over Regge geometries weighted by $e^{i\mathcal{I}}$ in the semiclassical regime.

These results are illustrated by the numerical analysis of the EPRL spinfoam amplitudes on triangulations Δ_3 and $\sigma_{1\text{-}5}$ (FIG.1(a) and (b)). As a byproduct, the "cosine problem" [25] is shown to be relaxed on Δ_3. Moreover, our results provide important evidence supporting the semiclassical consistency of the spinfoam theory.

2 Spinfoam amplitude

The 4-dimensional triangulation $\mathcal{K}$ contains 4-simplices v, tetrahedra e, triangles f, line segments, and points. We denote the internal triangle by h and the boundary triangle by b (f is either h or b), and assign the SU(2) spins $j_h, j_b \in \mathbb{N}_0/2$ to internal and boundary triangles h, b. The spin $j_f = j_h$ or j_b relates to the quantum area of f by $\mathfrak{a}_f = 8\pi\gamma G\hbar\sqrt{j_f(j_f+1)}$ [26, 27]. The Lorentzian EPRL spinfoam amplitude on $\mathcal{K}$ sums over internal spins $\{j_h\}$:

$$A(\mathcal{K}) = \sum_{\{j_h\}} \prod_h \boldsymbol{d}_{j_h} \int [\mathrm{d}g\mathrm{d}\mathbf{z}]\, e^{S(j_h, g_{ve}, \mathbf{z}_{vf}; j_b, \xi_{eb})}, \tag{2.1}$$

$$[\mathrm{d}g\mathrm{d}\mathbf{z}] = \prod_{(v,e)} \mathrm{d}g_{ve} \prod_{(v,f)} \mathrm{d}\Omega_{\mathbf{z}_{vf}}, \tag{2.2}$$

where $\boldsymbol{d}_{j_h} = 2j_h + 1$. The boundary states of $A(\mathcal{K})$ are SU(2) coherent states $|j_b, \xi_{eb}\rangle$ where $\xi_{eb} = u_{eb} \triangleright (1,0)^T$, $u_{eb} \in \mathrm{SU}(2)$. j_b, ξ_{eb} determines the area and the 3-normal of b in the boundary tetrahedron e. The summed/integrated variables are $g_{ve} \in \mathrm{SL}(2,\mathbb{C})$, $\mathbf{z}_{vf} \in \mathbb{CP}^1$, and j_h. The boundary j_b, ξ_{eb} are not summed/integrated. $\mathrm{d}g_{ve}$ is the $\mathrm{SL}(2,\mathbb{C})$ Haar measure. $\mathrm{d}\Omega_{\mathbf{z}_{vf}}$ is a scaling invariant measure on $\mathbb{CP}^1$. The spinfoam action S is complex, linear to j_h, j_b [15] and has the following expression,

$$S = \sum_{e'} j_h F_{(e',h)} + \sum_{(e,b)} j_b F^{in/out}_{(e,b)} + \sum_{(e',b)} j_b F^{in/out}_{(e',b)}, \tag{2.3}$$

$$F^{out}_{(e,b)} = 2\ln \frac{\langle Z_{veb}, \xi_{eb}\rangle}{\|Z_{veb}\|} + i\gamma \ln \|Z_{veb}\|^2, \tag{2.4}$$

$$F^{in}_{(e,b)} = 2\ln \frac{\langle \xi_{eb}, Z_{v'eb}\rangle}{\|Z_{v'eb}\|} - i\gamma \ln \|Z_{v'eb}\|^2, \tag{2.5}$$

$$F_{(e',f)} = 2\ln \frac{\langle Z_{ve'f}, Z_{v'e'f}\rangle}{\|Z_{ve'f}\|\,\|Z_{v'e'f}\|} + i\gamma \ln \frac{\|Z_{ve'f}\|^2}{\|Z_{v'e'f}\|^2}. \tag{2.6}$$

$Z_{vef} = g_{ve}^\dagger \mathbf{z}_{vf}$ and $f = h$ or b. e and e' are boundary and internal tetrahedra, respectively. Introducing the dual complex $\mathcal{K}^*$, the orientation of the face f^* dual to f induces ∂f^*'s orientation that is outgoing from the vertex dual to v and incoming to another vertex dual to v'. The logarithms are fixed to be the principal value. The spinfoam action has the following continuous gauge freedom:

- At each v, there is the $\mathrm{SL}(2,\mathbb{C})$ gauge freedom $g_{ve} \mapsto x_v^{-1} g_{ve}$, $\mathbf{z}_{vf} \mapsto x_v^\dagger \mathbf{z}_{vf}$, $x_v \in \mathrm{SL}(2,\mathbb{C})$. We fix one g_a to be a constant $\mathrm{SL}(2,\mathbb{C})$ matrix for each 4-simplex. The amplitude is independent of the choices of constant matrices.

- At each e, there is the $\mathrm{SU}(2)$ gauge freedom: $g_{v'e} \mapsto g_{v'e} h_e^{-1}$, $g_{ve} \mapsto g_{ve} h_e^{-1}$, $h_e \in \mathrm{SU}(2)$. To remove the gauge freedom, we set one of the group element $g_{v'e}$ along the edge e to be the upper triangular matrix. Indeed, any $g \in \mathrm{SL}(2,\mathbb{C})$ can be decomposed as $g = kh$ with $h \in \mathrm{SU}(2)$ and $k \in K$, where K is the subgroup of upper triangular matrices:

$$K = \left\{ k = \begin{pmatrix} \lambda^{-1} & \mu \\ 0 & \lambda \end{pmatrix},\ \lambda \in \mathbb{R} \setminus \{0\},\ \mu \in \mathbb{C} \right\}. \tag{2.7}$$

  We use the gauge freedom to set $g_{v'e} \in K$.

- $\mathbf{z}_{vf}$ can be computed by g_{ve} and ξ_{ef} up to a complex scaling: $\mathbf{z}_{vf} \propto_{\mathbb{C}} \left(g_{ve}^\dagger\right)^{-1} \xi_{ef}$. Each $\mathbf{z}_{vf}$ has the scaling gauge freedom $\mathbf{z}_{vf} \mapsto \lambda_{vf} \mathbf{z}_{vf}$, $\lambda_{vf} \in \mathbb{C}$. We fix the gauge by setting the first component of $\mathbf{z}_{vf}$ to 1. Then, the real critical point $\mathring{\mathbf{z}}_{vf}$ is in the form of $\mathring{\mathbf{z}}_{vf} = (1, \mathring{\alpha}_{vf})^T$, where $\mathring{\alpha}_{vf} \in \mathbb{C}$.

We have assumed the sum over internal $j_h \in \mathbb{N}_0/2$ in Eq.(2.1) is bounded by $j^{\max}$. For some internal triangles, h, $j^{\max}$ is determined by boundary spins j_b via the triangle inequality, or $j^{\max}$ is an IR cut-off in case of the bubble divergence.

Moreover, we would like to change the sum over j_h in Eq.(2.1) to the integral, preparing for the stationary phase analysis. The idea is to apply the Poisson summation formula. Firstly, we replace each $\boldsymbol{d}_{j_h}$ by a smooth compact support function $\tau_{[-\epsilon, j^{\max}+\epsilon]}(j_h)$ satisfying

$$\tau_{[-\epsilon, j^{\max}+\epsilon]}(j_h) = \boldsymbol{d}_{j_h}, \quad j_h \in [0, j^{\max}] \quad \text{and} \quad \tau_{[-\epsilon, j^{\max}+\epsilon]}(j_h) = 0, \quad j_h \notin [-\epsilon, j^{\max}+\epsilon], \tag{2.8}$$

for any $0 < \epsilon < 1/2$. This replacement does not change the value of the amplitude $A(\mathcal{K})$ but makes the summand of $\sum_{j_h}$ smooth and compact support in j_h. Applying the Poisson summation formula

$$\sum_{n \in \mathbb{Z}} f(n) = \sum_{k \in \mathbb{Z}} \int_{\mathbb{R}} \mathrm{d}n f(n)\, e^{2\pi i k n},$$

the discrete sum over j_h in $A(\mathcal{K})$ becomes integral. Therefore,

$$A(\mathcal{K}) = \sum_{\{k_h \in \mathbb{Z}\}} \int_{\mathbb{R}} \prod_h \mathrm{d}j_h \prod_h 2\tau_{[-\epsilon, j^{\max}+\epsilon]}(j_h) \int [\mathrm{d}g \mathrm{d}\mathbf{z}]\, e^{S^{(k)}}, \quad S^{(k)} = S + 4\pi i \sum_h j_h k_h. \tag{2.9}$$

By the area spectrum, the classical area $\mathfrak{a}_f$ and small $\hbar$ imply the large spin $j_f \gg 1$. This motivates to understand the large-j regime as the semiclassical regime of $A(\mathcal{K})$. To probe the semiclassical regime, we scale uniformly $\{j_b, j_h\} \to \{\lambda j_b, \lambda j_h\}$, where $\lambda \gg 1$. Scaling spins implies $S \to \lambda S$. Then, $A(\mathcal{K})$ is given by

$$A(\mathcal{K}) = \sum_{\{k_h \in \mathbb{Z}\}} \int \prod_h \mathrm{d}j_h \prod_h (2\lambda \boldsymbol{d}_{\lambda j_h}) \int [\mathrm{d}g \mathrm{d}\mathbf{z}]\, e^{\lambda S^{(k)}}, \tag{2.10}$$

$$S^{(k)} = S + 4\pi i \sum_h j_h k_h, \tag{2.11}$$

where j_h is real and continuous.

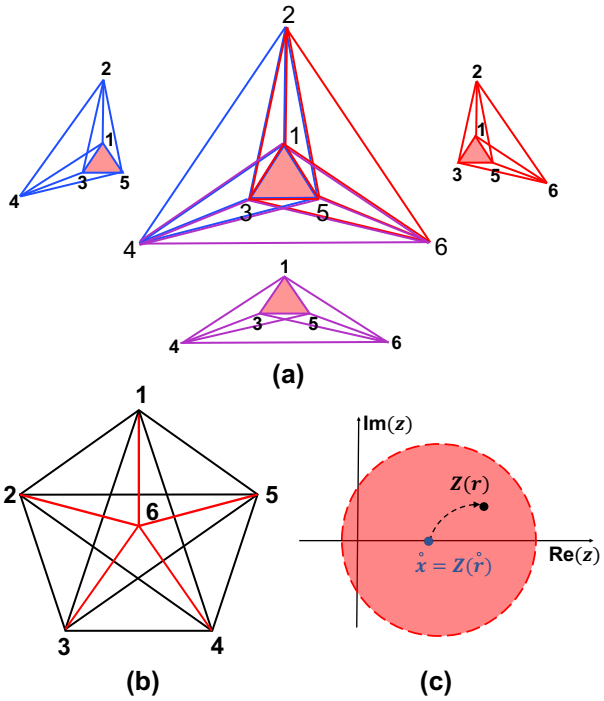

Figure 1. (a) The Δ_3 triangulation (the center panel) made by gluing three 4-simplices (in blue, red, and purple). The internal triangle (135) is highlighted in red. (b) The triangulation $\sigma_{1\text{-}5}$ made by the 1-5 Pachner move dividing a 4-simplex into five 4-simplices. $\sigma_{1\text{-}5}$ has 10 internal triangles and 5 internal segments $I = 1, \cdots, 5$ (red). (c) The real and complex critical points $\mathring{x}$ and $Z(r)$. $\mathcal{S}(r, z)$ is analytic extended from the real axis to the complex neighborhood illustrated by the red disk.

3 Real critical points and flatness.

For each k_h in (2.10), by the naive stationary phase approximation, the integral with $\lambda \gg 1$ is approximated by the dominant contributions from solutions of the critical equations

$$\mathrm{Re}(S) = \partial_{g_{ve}} S = \partial_{\mathbf{z}_{vf}} S = 0, \tag{3.1}$$

$$\partial_{j_h} S = 4\pi i k_h, \qquad k_h \in \mathbb{Z}. \tag{3.2}$$

The solution inside the integration domain is denoted by $\{\mathring{j}_h, \mathring{g}_{ve}, \mathring{\mathbf{z}}_{vf}\}$. We view the integration domain as a real manifold, and call $\{\mathring{j}_h, \mathring{g}_{ve}, \mathring{\mathbf{z}}_{vf}\}$ the *real critical point*.

Every solution satisfying the part (3.1) and a nondegeneracy condition endows a Regge geometry to $\mathcal{K}$ with 4d orientation [12–15]. Further imposing (3.2) to these Regge geometries gives the accidental flatness constraint to every deficit angle δ_h hinged by the internal triangle h [22, 23]

$$\gamma\delta_h = 4\pi k_h, \qquad k_h \in \mathbb{Z}. \tag{3.3}$$

The Barbero-Immirzi parameter $\gamma \neq 0$ is finite. When $k_h = 0$, δ_h at every internal triangle is zero, so the Regge geometry endowed by the real critical point is flat. If the dominant contribution to

$A(\mathcal{K})$ with $\lambda \gg 1$ only comes from real critical points, Eq.(3.3) implies that only the flat geometry and geometries with $\gamma\delta_h = \pm 4\pi\mathbb{Z}_+$ can contribute dominantly to $A(\mathcal{K})$, whereas the contributions from generic curved geometries are suppressed. If this was true, the semiclassical behavior of $A(\mathcal{K})$ would fail to be consistent with GR.

A generic $\{\mathring{j}_h, \mathring{g}_{ve}, \mathring{\mathbf{z}}_{vf}\}$ can endow discontinuous 4d orientation, i.e., the orientation flips between 4-simplices. Then (3.3) becomes $\gamma \sum_{v\in h} s_v \Theta_h(v) = 4\pi k_h$ where $s_v = \pm 1$ labels two possible orientations at each 4-simplex v. $\Theta_h(v)$ is the dihedral angle hinged by h in v.

4 Complex critical points.

As we will show, the large-λ spinfoam amplitude does receive non-suppressed contributions from curved geometries with small but nonzero $|\delta_h|$. Demonstrating this property needs a more refined stationary phase analysis of the spinfoam amplitude: We come back to the amplitude (2.10) and separate M internal areas j_{h_o} ($h_o = 1, \cdots, M$) from other internal areas $j_{\bar{h}}$ ($\bar{h} = 1, \cdots, F - M$). F is the total number of internal triangles. M equals to number of internal segments I in $\mathcal{K}$. The areas $\{j_{h_o}\}$ are suitably chosen such that we can change variables from $\{j_{h_o}\}_{h_o=1}^M$ to internal segment-lengths $\{l_I\}_{I=1}^M$ (by inverting Heron's formula [1]) in a neighborhood of $\{\mathring{j}_{h_o}\}$ of a real critical point $\{\mathring{j}_h, \mathring{g}_{ve}, \mathring{\mathbf{z}}_{vf}\}$. $\mathrm{d}^{M+N} j_h = \mathcal{J}_l \mathrm{d}^M l_I \, \mathrm{d}^{F-M} j_{\bar{h}}$ where $\mathcal{J}_l$ is the jacobian.

$$A(\mathcal{K}) = \sum_{\{k_h\}} \int \prod_{I=1}^{M} \mathrm{d}l_I \mathcal{Z}_{\mathcal{K}}^{\{k_h\}}(l_I), \tag{4.1}$$

$$\mathcal{Z}_{\mathcal{K}}^{\{k_h\}}(l_I) = \int \prod_{\bar{h}} \mathrm{d}j_{\bar{h}} \prod_h (2\lambda \boldsymbol{d}_{\lambda j_h}) \int [\mathrm{d}g \mathrm{d}\mathbf{z}] e^{\lambda S^{(k)}} \mathcal{J}_l, \tag{4.2}$$

The partial amplitude $\mathcal{Z}_{\mathcal{K}}^{\{k_h\}}$ have the external parameters $r \equiv \{l_I, j_b, \xi_{eb}\}$ including not only the boundary data but also internal segment-lengths l_I. To study $\mathcal{Z}_{\mathcal{K}}^{\{k_h\}}$, we apply the stationary phase analysis for the complex action with parameters [28, 29]: We consider the large-λ integral $\int_K e^{\lambda S(r,x)} \mathrm{d}^N x$, and regard r as parameters. $S(r,x)$ is an analytic function of $r \in U \subset \mathbb{R}^k, x \in K \subset \mathbb{R}^N$. $U \times K$ is a neighborhood of $(\mathring{r}, \mathring{x})$. $\mathring{x}$ is a real critical point of $S(\mathring{r}, x)$. $\mathcal{S}(r,z)$, $z = x + iy \in \mathbb{C}^N$, is the analytic extension of $S(r,x)$ to a complex neighborhood of $\mathring{x}$. The complex critical equation $\partial_z \mathcal{S} = 0$ is solved by $z = Z(r)$ where $Z(r)$ is an analytic function of r in the neighborhood U. When $r = \mathring{r}$, $Z(\mathring{r}) = \mathring{x}$ reduces to the real critical point. When r deviates away from $\mathring{r}$, $Z(r) \in \mathbb{C}^N$ can move away from the real plane $\mathbb{R}^N$, thus is called the *complex critical point* (see FIG.1(b)). We have the following large-λ asymptotic expansion for the integral

$$\int_K e^{\lambda S(r,x)} \mathrm{d}^N x = \left(\frac{1}{\lambda}\right)^{\frac{N}{2}} \frac{e^{\lambda \mathcal{S}(r,Z(r))}}{\sqrt{\det\left(-\delta_{z,z}^2 \mathcal{S}(r,Z(r))/2\pi\right)}} \times [1 + O(1/\lambda)] \tag{4.3}$$

where $\mathcal{S}(r,Z(r))$ and $\delta_{z,z}^2 \mathcal{S}(r,Z(r))$ are the action and Hessian at the complex critical point.

The crucial information of (4.3) is: the integral can receive the dominant contribution from the complex critical point away from the real plane. This fact has been overlooked by the argument of

[1] We relate the chosen M areas $\{j_{h_o}\}$ to M segment-lengths $\{l_I\}$ by Heron's formula as in Regge geometry. Inverting the relation between $\{j_{h_o}\}_{h_o=1}^M$ and $\{l_I\}_{I=1}^M$ defines the change of variables $(j_{h_o}, j_{\bar{h}}) \to (l_I, j_{\bar{h}})$ in a neighborhood of the real critical point. This procedure is just changing variables and does not impose any restriction.

the flatness problem. Moreover, Eq.(4.3) reduces $A(\mathcal{K})$ to the integral

$$\left(\frac{1}{\lambda}\right)^{\frac{N}{2}} \int \prod_{I=1}^{M} \mathrm{d}l_I \mathscr{N}_l \, e^{\lambda \mathcal{S}(r,Z(r))} \left[1 + O(1/\lambda)\right] \tag{4.4}$$

at each k_h. $\mathscr{N}_l \propto \prod_h (4j_h)\, \mathcal{J}_l[\det(-\delta^2_{z,z}\mathcal{S}/2\pi)]^{-1/2}$ at $Z(r)$. Given that $\{l_I\}$ determines the Regge geometry on $\mathcal{K}$, Eq.(4.4) describes the dynamics of Regge geometries with the effective action $\mathcal{S}$, which does not exclude curved geometries. In the following, we make the above general analysis concrete by considering 2 examples of spinfoam amplitudes on $\mathcal{K} = \Delta_3, \sigma_{1\text{-}5}$, and we compute numerically the complex critical points and $\mathcal{S}$, confirming the resolution of the flatness problem.

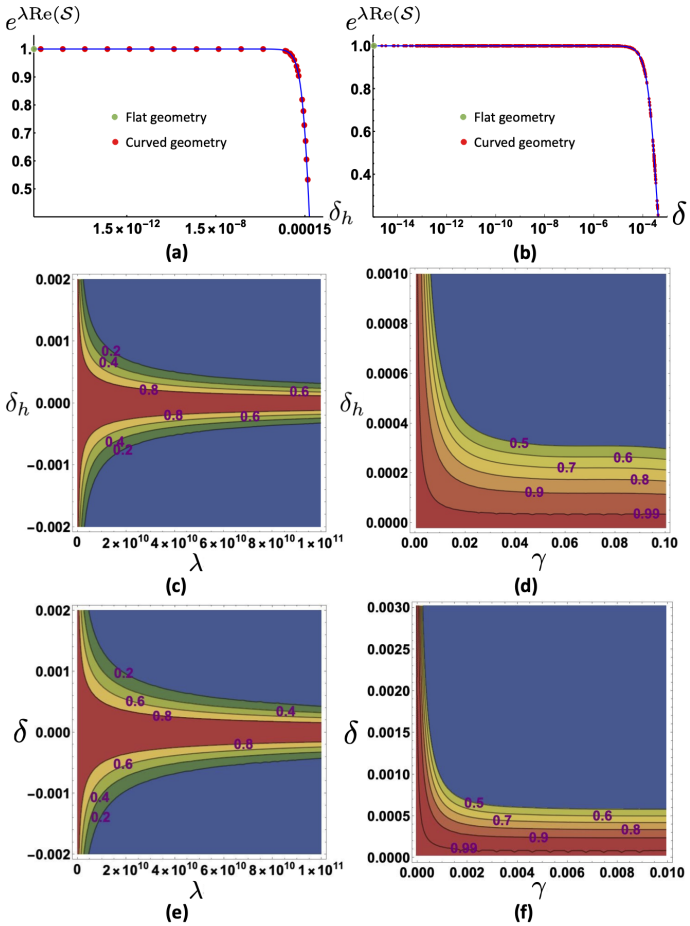

Figure 2. (a) plots $e^{\lambda \mathrm{Re}(\mathcal{S})}$ versus the deficit angle δ_h at $\lambda = 10^{11}$ and $\gamma = 0.1$ in $A(\Delta_3)$, and (b) plots $e^{\lambda \mathrm{Re}(\mathcal{S})}$ versus the deficit angle $\delta = \sqrt{\frac{1}{10}\sum_{h=1}^{10} \delta_h^2}$ at $\lambda = 10^{11}$ and $\gamma = 1$ in $\mathcal{Z}_{\sigma_{1-5}}$. These 2 plots show the numerical data of curved geometries (red points) and the best fits (5.8) and (6.4) (blue curve). (c) and (d) are the contour plots of $e^{\lambda \mathrm{Re}(\mathcal{S})}$ as functions of (λ, δ_h) at $\gamma = 0.1$ and of (γ, δ_h) at $\lambda = 5 \times 10^{10}$ in $A(\Delta_3)$. (e) and (f) are the contour plots of $e^{\lambda \mathrm{Re}(\mathcal{S})}$ as functions of (λ, δ) at $\gamma = 1$ and of (γ, δ) at $\lambda = 5 \times 10^{10}$ in $\mathcal{Z}_{\sigma_{1\text{-}5}}$. They demonstrate the (non-blue) regime of curved geometries where the spinfoam amplitude is not suppressed.

5 Asymptotics of $A(\Delta_3)$

We firstly focus on a simpler example $A(\Delta_3)$ where Δ_3 contains three 4-simplices and a single internal triangle h. All line segments of Δ_3 are at the boundary, so $M = 0$ in (4.1). The Regge geometry $\mathbf{g}$ on Δ_3 is fixed by the (Regge-like) boundary data $\{j_b, \xi_{eb}\}$ that uniquely corresponds to the boundary segment-lengths.

Translate the above general theory to $A(\Delta_3)$: $r = \{j_b, \xi_{eb}\}$ is the boundary data. $\mathring{r} = \{\mathring{j}_b, \mathring{\xi}_{eb}\}$ determines the flat geometry $\mathbf{g}(\mathring{r})$ with $\delta_h = 0$. $\mathring{x} = \{\mathring{j}_h, \mathring{g}_{ve}, \mathring{\mathbf{z}}_{vf}\}$ is the real critical point associated to $\mathring{r}$ and endows the orientations $s_v = +1$ to all 4-simplices. $\mathring{r}$, $\mathbf{g}(\mathring{r})$, and $\mathring{x}$ are computed numerically in A.1 and A.2. The integration domain of $A(\Delta_3)$ is 124 real dimensional. We define local coordinates $x \in \mathbb{R}^{124}$ covering the neighborhood of $\mathring{x}$ inside the integration domain (see A.3). $S(r, x)$ is the spinfoam action, analytic in the neighborhood of $(\mathring{r}, \mathring{x})$. $z \in \mathbb{C}^{124}$ complexifies x. $\mathcal{S}(r, z)$ extends holomorphically $S(r, x)$ to a complex neighborhood of $\mathring{x}$. We only complexify x but do not complexify r. We focus on $k_h = 0$, and the different regimes of the boundary data r result in different large-λ asymptotic behavior of $A(\Delta_3)$.

- Regime 1: fixing the boundary data $r = \mathring{r}$, A.2 gives numerically the real critical point for the flat geometry $\mathbf{g}(\mathring{r})$, whose deficit angle is $\delta_h = 0$. $e^{S(\mathring{r},\mathring{x})}$ evaluated at the real critical points $\mathring{x}$ gives the dominant contribution to the asymptotic amplitude.

$$\int \mathrm{d}^N x\, \mu(x)\, e^{\lambda S(\mathring{r},x)} \sim \left(\frac{1}{\lambda}\right)^{\frac{N}{2}} \frac{e^{\lambda S(\mathring{r},\mathring{x})}\mu(\mathring{x})}{\sqrt{\det\left(-\delta^2_{x,x} S(r,\mathring{x})/2\pi\right)}} \left[1 + O(1/\lambda)\right]. \tag{5.1}$$

  The asymptotics behaves as a power law in $1/\lambda$. Here we only focus on the contribution from the single real critical point $\mathring{x}$. There is another real critical point which we will discuss in a moment.

- Regime 2: fixing the boundary data r which determine the segment-lengths for a curved geometry $\mathbf{g}(r)$, the real critical point is absent, then the integral is suppressed faster than any polynomial in $1/\lambda$:

$$\int \mathrm{d}^N x\, \mu(x)\, e^{\lambda S(r,x)} = O(\lambda^{-K}), \quad \forall\, K > 0. \tag{5.2}$$

The above asymptotic behavior is based on fixing r and sending λ to be large. However, in order to clarify contributions from curved geometries and compare them to the contribution from the flat geometry, we should also let r vary and have an interpolation between two regimes (5.1) and (5.2). This motivates us to use the complex critical point of the analytically continued action $\mathcal{S}(r, z)$. We vary the length l_{26} of the line segment connecting the points 2 and 6, leaving other segment lengths unchanged. A family of (Regge-like) boundary data $r = \mathring{r} + \delta r$ parametrized by l_{26} is obtained numerically, and gives the family of curved geometries $\mathbf{g}(r)$ with $\delta_h \neq 0$ (see A.4).

At each r, the real critical point is absent. But we find the complex critical point $z = Z(r)$ satisfying $\partial_z \mathcal{S}(r, z) = 0$ with high-precision numerics. At each curved geometry $\mathbf{g}(r)$, the real critical point is absent for $\delta_h \neq 0$. We numerically compute the complex critical point $Z(r)$ satisfying the complex critical equations $\partial_z \mathcal{S}(r, z) = 0$ with Newton-like recursive procedure. First, we linearize $\partial_z \mathcal{S}(r, z) = 0$ at the pseudo-critical point $x_0 \in \mathbb{R}^{124}$. Then, we have the linear system of equations

$$\partial^2_{z,z} \mathcal{S}(r, x_0) \cdot \delta z_1 + \partial_z \mathcal{S}(r, x_0) \simeq 0, \tag{5.3}$$

We obtain $z_1 = x_0 + \delta z_1$ by the solution δz_1. We again linearize $\partial_z \mathcal{S}(r,z) = 0$ at z_1,

$$\partial^2_{z,z} \mathcal{S}(r, z_1) \cdot \delta z_2 + \partial_z \mathcal{S}(r, z_1) \simeq 0, \tag{5.4}$$

we obtain $z_2 = z_1 + \delta z_2$ by the solution δz_2. We iterate and linearize the complex critical equations at $z_2, z_3, \cdots, z_{n-1}$. The resulting $z_n = z_{n-1} + \delta z_n$ should approximates the complex critical points $Z(r)$ arbitrarily well for sufficiently large n. In practise, $n = 4$ turns out to be sufficient for our calculation. The numerical results of complex critical point for each geometry r can be found in Mathematica notebook [30].

The absolute error of numerically solving $\partial_z \mathcal{S}(r,z) = 0$ is measured by

$$\varepsilon = \max \left| \partial_z \mathcal{S}(r, z_n) \right| . \tag{5.5}$$

We have z_n well-approximate the complex critical point $Z(r)$ if ε is small (see A.5).

We insert $Z(r)$ into $\mathcal{S}(r,z)$, and compute numerically the difference between $\mathcal{S}(r, Z(r))$ and the Regge action $\mathcal{I}_R$ of the *curved* geometry $\mathbf{g}(r)$:

$$\delta\mathcal{I}(r) \;=\; \mathcal{S}(r, Z(r)) - i\mathcal{I}_R[\mathbf{g}(r)], \tag{5.6}$$

$$\text{where} \quad \mathcal{I}_R[\mathbf{g}(r)] = \mathfrak{a}_h(r)\delta_h(r) + \sum_b \mathfrak{a}_b(r)\Theta_b(r). \tag{5.7}$$

The areas $\mathfrak{a}_h(r), \mathfrak{a}_b(r)$ and deficit/dihedral angles $\delta_h(r)$,$\Theta_b(r)$ are computed from $\mathbf{g}(r)$.

We repeat the computation for many r from varying l_{26}. The computations give a family of $\delta\mathcal{I}(r)$. We relate $\delta\mathcal{I}(r)$ to $\delta_h(r)$ and find the best polynomial fit (see FIG.2(a))

$$\delta\mathcal{I} = a_2(\gamma)\delta_h^2 + a_3(\gamma)\delta_h^3 + a_4(\gamma)\delta_h^4 + O(\delta_h^5), \tag{5.8}$$

The coefficients a_i at $\gamma = 0.1$ are given in A.5.

By (4.3), the dominant contribution from $Z(r)$ to $A(\Delta_3)$ is proportional to $|e^{i\lambda\mathcal{S}}| = e^{\lambda \mathrm{Re}(\mathcal{S})} \leq 1$. As shown in FIG.2(a) and (c), given any finite $\lambda \gg 1$, there are curved geometries with small nonzero $|\delta_h|$ such that $|A(\Delta_3)|$ is the same order of magitude as $|A(\Delta_3)|$ at the flat geometry. The range of δ_h for non-suppressed $A(\Delta_3)$ is nonvanishing as far as λ is finite. The range of δ_h is enlarged when γ is small, shown in FIG.2(d).

We remark that the semiclassical behavior of the spinfoam amplitude is given by the $1/\lambda$ expansion as (4.3) with finite λ. It is similar to quantum mechanics, where $\hbar$ is finite, and the classical mechanics is reproduced by the $\hbar$-expansion. The finite λ leads to the finite range of nonvanishing δ_h.

So far we have considered the real critical point $\mathring{x}$ of the flat geometry with all $s_v = +1$. Given the boundary data $\mathring{r}$, there are exactly 2 real critical points $\mathring{x}$ and $\mathring{x}'$, where $\mathring{x}'$ corresponds to the same flat geometry but with all $s_v = -1$. Other 6 discontinuous orientations (two 4-simplices has plus/minus and the other has minus/plus) do not leads to any real critical point (see Figure 3 and A.6 for δ_h^s values), because they all violates the flatness constraint $\gamma\delta_h^s = \gamma \sum_v s_v \Theta_h(v) = 0$. $|\delta_h^s|$ is not small for the discontinuous orientation, so the contribution to $A(\Delta_3)$ is suppressed even when considering the complex critical point.

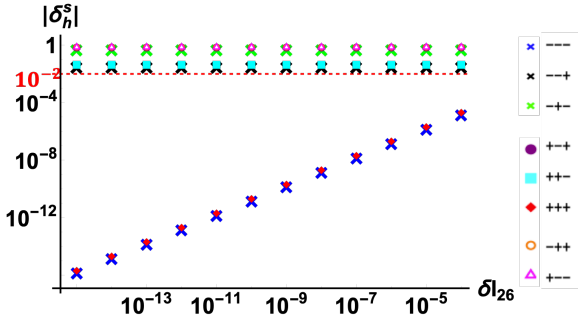

Figure 3. The Log-Log plot of $|\delta_h^s|$ for different $s = \{s_v\}_v$ when varying $l_{26} = \mathring{l}_{26} + \delta l_{26}$.

We focus on the integrals over 2 real neighborhoods K, K' of $\mathring{x}, \mathring{x}'$, since the integral outside $K \cup K'$ only gives suppressed contribution to $A(\Delta_3)$ for large λ. The above analysis is for the integral over K. We carry out a similar analysis for the integral over K'. The following asymptotic formula of $A(\Delta_3)$ is obtained with $r = \mathring{r} + \delta r$ of curved geometries $\mathbf{g}(r)$

$$A(\Delta_3) = \left(\frac{1}{\lambda}\right)^{60} \left[\mathscr{N}_+ e^{i\lambda \mathcal{I}_R[\mathbf{g}(r)]+\lambda\delta\mathcal{I}(r)} + \mathscr{N}_- e^{-i\lambda \mathcal{I}_R[\mathbf{g}(r)]+\lambda\delta\mathcal{I}'(r)}\right][1 + O(1/\lambda)]\,. \tag{5.9}$$

up to an overall phase. 2 complex critical points in complex neighborhoods of $\mathring{x}, \mathring{x}'$ contribute dominantly and give respectively 2 terms, with phase plus or minus the Regge action of the curved geometry $\mathbf{g}(r)$ plus curvature corrections $\delta\mathcal{I}(r)$ in (5.8) and $\delta\mathcal{I}'(r) = \delta\mathcal{I}(r)^*|_{\delta_h \to -\delta_h}$. $\mathscr{N}_\pm$ are proportional to $[\det(-\delta^2_{z,z}\mathcal{S}/2\pi)]^{-1/2}$ evaluated at these 2 complex critical points (see A.6).

As an example of the suspected *cosine problem* [25], there has been the guess $A(\Delta_3) \sim (\mathscr{N}_1 e^{i\lambda\mathcal{I}_R} + \mathscr{N}_2 e^{-i\lambda\mathcal{I}_R})^3$ (each factor is from the vertex amplitude, see e.g. [31]) whose expansion gives 8 terms corresponding to all possible orientations. But Eq.(5.9) demonstrates that $A(\Delta_3)$ only contain 2 terms corresponding to the continuous orientations. The cosine problem is relaxed.

6 1-5 Pachner move

$\sigma_{1\text{-}5}$ is the complex of the 1-5 Pachner move refining a 4-simplex into five 4-simplices (see B.1). $\sigma_{1\text{-}5}$ has 5 internal segments $I = 1, \cdots, 5$ (see FIG.1(b)), in contrast to Δ_3 where all segments are at the boundary. There are 10 internal triangles h in $\sigma_{1\text{-}5}$. The spinfoam amplitude $A(\sigma_{1\text{-}5})$ is given by (4.1) with $M = 5$ and $F = 10$. We consider $\{\mathring{j}_h, \mathring{g}_{ve}, \mathring{\mathbf{z}}_{vf}\}$ as a real critical point of flat geometry on $\sigma_{1\text{-}5}$. The flat geometry on $\sigma_{1\text{-}5}$ is not unique. The position of P_6 can move continuously in $\mathbb{R}^4$ to lead to the continuous family of flat geometries on $\sigma_{1\text{-}5}$. The continuous family of flat geometries result in the continuous family of real critical points. It implies that all these real critical points lead to degenerate Hessian matrices, in contrast to $A(\Delta_3)$ where the real critical point is nondegenerate. Therefore we develop the following additional procedure to generalize the analysis from Δ_3 to $\sigma_{1\text{-}5}$.

We label boundary spins j_{mnk} by a triple of points $m \neq n \neq k = 1, 2, \cdots, 5$, and label the internal spins j_{mn6} by $m, n = 1, 2, \cdots, 5$ and point 6. The dual faces and spins are labelled in the dual cable diagram Fig.4(b). We pick up 5 internal spins j_{126}, j_{136}, j_{146}, j_{156}, j_{236} and their corresponding integrals in $A(\sigma_{1\text{-}5})$. The integrand is denoted by $\mathcal{Z}_{\sigma_{1\text{-}5}}$. Namely

$$A(\sigma_{1\text{-}5}) = \int_{\mathbb{R}^5} \mathrm{d}j_{126}\mathrm{d}j_{136}\mathrm{d}j_{146}\mathrm{d}j_{156}\mathrm{d}j_{236}\, \mathcal{Z}_{\sigma_{1\text{-}5}}(j_{126}, j_{136}, j_{146}, j_{156}, j_{236})\,, \tag{6.1}$$

$$\mathcal{Z}_{\sigma_{1\text{-}5}} = \sum_{\{k_h\}} \int_{\mathbb{R}^5} \prod_{\bar{h}=1}^{5} \mathrm{d}j_{\bar{h}} \prod_{h=1}^{10} 2\lambda\, \tau_{[-\epsilon, \lambda j^{\max}+\epsilon]}(\lambda j_h) \int [\mathrm{d}g\mathrm{d}\mathbf{z}] e^{\lambda S^{(k)}}\,, \tag{6.2}$$

where other five internal spins j_{246}, j_{256}, j_{346}, j_{356}, j_{456} are denoted by $j_{\bar{h}}$ ($\bar{h}=1,2,\cdots,5$). At the real critical point constructed above, the 5 areas $\mathring{j}_{126}$, $\mathring{j}_{136}$, $\mathring{j}_{146}$, $\mathring{j}_{156}$, $\mathring{j}_{236}$ are determined by the internal segment-lengths $\mathring{l}_{m6}$ ($m=1,2,\cdots,5$) via the Heron's formula. We focus on a neighborhood of $(j_{126}, j_{136}, j_{146}, j_{156}, j_{236})\in\mathbb{R}^5$ around $(\mathring{j}_{126}, \mathring{j}_{136}, \mathring{j}_{146}, \mathring{j}_{156}, \mathring{j}_{236})$ such that the five j's in the neighborhood uniquely correspond to the five segment-lengths l_{m6}, $m=2,\cdots,5$.

We generalize the analysis of $A(\Delta_3)$ to $\mathcal{Z}_{\sigma_{1\text{-}5}}$. $\mathcal{Z}_{\sigma_{1\text{-}5}}$ in Eq.(6.2) contain integrals with the external parameters

$$r=\{j_{126}, j_{136}, j_{146}, j_{156}, j_{236}, j_b, \xi_{eb}\} \tag{6.3}$$

which including not only boundary data but also 5 internal j's. We focus on the integral in $\mathcal{Z}_{\sigma_{1\text{-}5}}$ at $k_h=0$. Given $r=\mathring{r}=\{\mathring{j}_{126}, \mathring{j}_{136}, \mathring{j}_{146}, \mathring{j}_{156}, \mathring{j}_{236}, \mathring{j}_b, \mathring{\xi}_{eb}\}$, the integral has the real critical point $\{\mathring{j}_{\bar{h}}, \mathring{g}_a, \mathring{\mathbf{z}}_{a,b}\}$ corresponding to the flat geometry $\mathbf{g}(\mathring{r})$. The data of $\mathring{r}$ and the real critical point are given in B.1. The Hessian matrix at $\mathring{x}$ is nondegenerate in $\mathcal{Z}_{\sigma_{1\text{-}5}}$, as confirmed by the numerical check.

The similar parametrizations in A.3 for $g_a, \mathbf{z}_{a,b}, j_{\bar{h}}$ define the local coordinates $x\in\mathbb{R}^{195}$ covering a neighborhood K of $\mathring{x}=(0,0,\cdots,0)$. We again express the spinfoam action as $S(r,x)$. The integral in $\mathcal{Z}_{\sigma_{1\text{-}5}}$ is of the same type as (A.16) with $N=195$.

To give the curved geometries, we fix the boundary data $\mathring{j}_b, \mathring{\xi}_{eb}$ and deform the 5 internal segment-lengths $l_{m6}=\mathring{l}_{m6}+\delta l_{m6}$, $m=1,\cdots,5$. We randomly sample δl_{m6} in the range 10^{-15} to 10^{-5}. Each time, for the each new internal segment-lengths l_{m6}, we can repeat the procedure in B.1 to reconstruct the geometry and compute all the geometric quantities of triangulation: e.g. the areas, the 4-d normals of each tetrahedron, and the deficit angles. Some data of the deformation $\delta l_{m6}=(\delta l_{16}, \delta l_{26}, \delta l_{36}, \delta l_{46}, \delta l_{56})$ and the corresponding deficit angles δ_h are shown in B.2.

Fixing $\mathring{j}_b, \mathring{\xi}_{eb}$, varying $l_{m6}=\mathring{l}_{m6}+\delta l_{m6}$ results in varying the 5 areas in r e.g. $j_{126}=\mathring{j}_{126}+\delta j_{126}$, $j_{136}=\mathring{j}_{136}+\delta j_{136},\cdots$. Thus we obtain the deformation of external data $r=\mathring{r}+\delta r$ of $\mathcal{Z}_{\sigma_{1\text{-}5}}$. We denote by r_l the external data obtained by sampling δl_{m6}, and denote the Regge geometries by $\mathbf{g}(r_l)$. There are 4 degrees of freedom of δl_{m6} still resulting in flat geometries, whereas there is 1 degree of freedom of δl_{m6} resulting in curved geometries.

We apply the Newton-like recursive method to numerically compute complex critical points $Z(r_l)$ for all r_l, the absolute errors are shown in B.3. $Z(r_l)$ is still in the real plane if r_l corresponds to the flat geometry, whereas $Z(r_l)$ is away from the real plane if r_l corresponds to the curved geometry. Once we have complex critical points $Z(r_l)$ for the curved geometries $\mathbf{g}(r_l)$, we numerically compute the analytic continued action $\mathcal{S}(r_l, Z(r_l))$ at complex critical points and the difference $\delta\mathcal{I}(r_l)=\mathcal{S}(r_l, Z(r_l))-S(r_l, x_0)$ where x_0 is the pseudo-critical point of $S(r_l, x)$. We have $S(r_l, x_0)=-i\mathcal{I}_R[\mathbf{g}(r)]+i\varphi$, where φ only relates to the boundary data and is independent of l_{m6} as confirmed by numerical tests (see also [14] for the analytic argument). The result of $|e^{i\lambda\mathcal{S}}|=e^{\lambda\mathrm{Re}(\mathcal{S})}$ is presented in FIG.2 (b), (e), and (f), which demonstrate curved geometries with small $|\delta_h|$ do not lead to the suppression of $\mathcal{Z}_{\sigma_{1\text{-}5}}(l_I)$. Moreover $\mathcal{S}(r_l, Z(r_l))$ is numerically fit by (see B.3):

$$\mathcal{S}(r_l, Z(r_l))=-i\mathcal{I}_R[\mathbf{g}(r_l)]-a_2(\gamma)\delta(r_l)^2+O(\delta^3), \tag{6.4}$$

where $\delta(r_l)=\sqrt{\frac{1}{10}\sum_{h=1}^{10}\delta_h(r_l)^2}$ and $a_2=-0.033i+8.88\times10^{-5}$ at $\gamma=1$. $\mathcal{I}_R[\mathbf{g}(r_l)]$ is the Regge action of $\mathbf{g}(r_l)$. As a result, we obtain the following large-λ contribution to $\mathcal{Z}_{\sigma_{1\text{-}5}}$ and $A(\sigma_{1\text{-}5})$ from the neighborhood around $(\mathring{r},\mathring{x})$

$$\mathcal{Z}_{\sigma_{1\text{-}5}}\sim\left(\frac{1}{\lambda}\right)^{\frac{155}{2}}e^{i\lambda\varphi}\mathscr{N}_l'\,e^{-i\lambda\mathcal{I}_R[\mathbf{g}(r_l)]-\lambda a_2(\gamma)\delta(r_l)^2+O(\delta^3)}\left[1+O(1/\lambda)\right], \tag{6.5}$$

$$A(\sigma_{1\text{-}5}) \sim \left(\frac{1}{\lambda}\right)^{\frac{155}{2}} e^{i\lambda\varphi} \int \prod_{m=1}^{5} \mathrm{d}l_{m6} \mathscr{N}_l \, e^{-i\lambda \mathcal{I}_R[\mathbf{g}(r_l)] - \lambda a_2(\gamma)\delta(r_l)^2 + O(\delta^3)} \left[1 + O(1/\lambda)\right], \qquad (6.6)$$

where we have made the local changes of variables from j_{126}, j_{136}, j_{146}, j_{156}, j_{236} to l_{m6}, and the Jacobian $\mathcal{J}_l = |\det(\partial j/\partial l)|$ (see B.3) is absorbed in $\mathscr{N}_l = \mathcal{J}_l \mathscr{N}_l'$. The spinfoam amplitude $A(\sigma_{1\text{-}5})$ reduces to the integral over geometries $\mathbf{g}(r_l)$ in the semiclassical regime.

7 Discussion

Our results resolve the flatness problem by demonstrating explicitly the curved Regge geometries emergent from the large-j EPRL spinfoam amplitudes. The curved geometries correspond to complex critical points that are away from the real integration domain. They give non-suppressed $e^{\lambda \mathrm{Re}(\mathcal{S})}$ and satisfy the bound $\mathrm{Re}(a_2(\gamma))\delta^2 \lesssim 1/\lambda$, if we consider the examples (5.8) and (6.4) neglecting $O(\delta^3)$. This bound is consistent with the earlier proposal [23] and the result in the effective spinfoam model [32–34], although this bound should be corrected when taking into account $O(\delta_h^3)$ in (5.8) and (6.4). The similar bound should be valid to the spinfoam amplitude in general.

All resulting curved geometries are of small deficit angles δ_h. The large-j spinfoam amplitude is still suppressed for geometries with larger δ_h violating the above bound. This is not a problem for the semiclassical analysis. Indeed, non-singular classical spacetime geometries are smooth with vanishing δ_h. To well-approximating smooth geometries by Regge geometries, the triangulation must be sufficiently refined, and all δ_h's must be small.

The confusion in the flatness problem can be seen as a wrong order of limits: If one fixes the triangulation first, one can find boundary data for which the amplitude goes wrong for large λ. But this is the wrong limit. The right one is: for each boundary data (hence each λ), there is a triangulation for which the amplitude gives a good result to any desired accuracy [35, 36].

Lastly, the 1-5 pachner move is the elementary step for the triangulation refinement. Our results provide a new routine for analyzing triangulation dependence in spinfoam models. This should closely relate to the spinfoam renormalization [37–39], with the goal to address the issue of triangulation-dependence.

Acknowledgements

The authors acknowledge Jonathan Engle, Francesco Gozzini, Wojciech Kaminski, and Carlo Rovelli for helpful discussions and comments. M.H. receives support from the National Science Foundation through grant PHY-1912278. Z.H. is supported by Xi De post-doc funding from State Key Laboratory of Surface Physics at Fudan University.

A The spinfoam amplitude $A(\Delta_3)$

A.1 The flat geometry on Δ_3

The Δ_3 triangulation is made by three 4-simplices sharing a common triangle. Δ_3 has 18 boundary triangles and one internal triangle. All line segments of Δ_3 are at the boundary, and the segment-lengths $l_{ab}(a \neq b = 1, 2, 3, 4, 5, 6)$ determine the Regge geometry $\mathbf{g}(r)$ ($\mathbf{g}(r)$ does not contain the information of the 4-simplex orientations).

The dual cable diagram for the Δ_3 triangulation is represented in FIG.4(a). Each box in FIG.4 carries group variables $g_a \in \mathrm{SL}(2,\mathbb{C})$ [2]. Each strand carries an SU(2) spin $j_{a,b}$ where a, b corresponds

[2]For convenience, the indexes of group variables in FIG. 4(a) are $a = 1, 2, 3..., 15$, the corresponding tetrahedra e are labeled by the number circles in FIG.1(a). The correspondence are: $g_1 \to e_{2,3,4,5}$, $g_2 \to e_{1,2,4,5}$, $g_3 \to e_{1,2,3,4}$, $g_4 \to e_{1,3,4,5}$, $g_5 \to e_{1,2,3,5}$, $g_6 \to e_{1,2,3,5}$, $g_7 \to e_{1,2,5,6}$, $g_8 \to e_{1,3,5,6}$, $g_9 \to e_{1,2,3,6}$, $g_{10} \to e_{2,3,5,6}$, $g_{11} \to e_{1,3,5,6}$, $g_{12} \to e_{1,3,4,5}$, $g_{13} \to e_{1,4,5,6}$, $g_{14} \to e_{1,3,4,6}$, $g_{15} \to e_{3,4,5,6}$.

to 2 different tetrahedra sharing the same 4-simplex. We have the identification $j_{a,b}$'s along the same strand, e.g. $j_{2,5} = j_{6,7}$ along the pink strand. The red strands dual to the common triangle shared by three 4-simplices. We use j_h to denote the spin $j_{4,5} = j_{6,8} = j_{11,12}$ of the internal triangle. The circles at the ends of the strands represent the SU(2) coherent states.

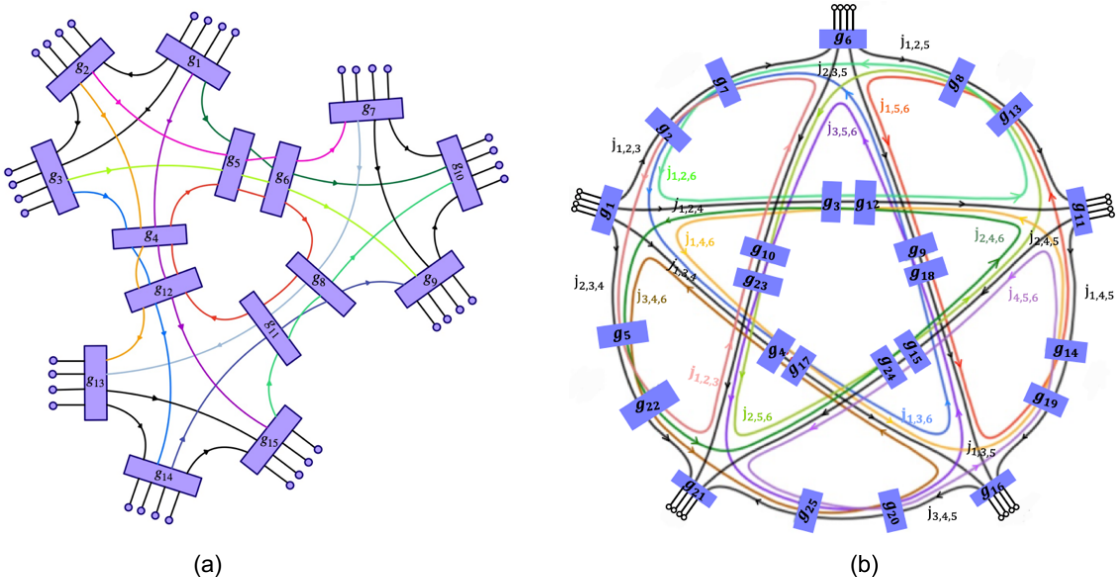

Figure 4. (a). The dual cable diagram of the Δ_3 spinfoam amplitude: The boxes correspond to tetrahedra carrying $g_a \in \mathrm{SL}(2,\mathbb{C})$. The strands stand for triangles carrying spins j_f. The strand with the same color belonging to different dual vertex corresponds to the triangle shared by the different 4-simplices. The circles as the endpoints of the strands carry boundary states $|j_b, \xi_{eb}\rangle$. The arrows represent orientations. This figure is adapted from [19]. (b). The dual cable diagram of the 1-5 pachner move amplitude. The internal faces are colored loops carrying internal spins j_h. The boundary faces are black strands carrying boundary spins j_b. The arrows represent orientations. This figure is adapted from [39].

We firstly construct the flat Regge geometry on Δ_3, in order to obtain the corresponding boundary data $\mathring{r} = \{\mathring{j}_b, \mathring{\xi}_{eb}\}$ and compute the associated real critical point $\mathring{x}$. We set the 6 points of Δ_3 in $\mathbb{R}^4$ as

$$\begin{aligned} P_1 = (0,0,0,0), P_2 = \left(0, -2\sqrt{10}/3^{3/4}, -\sqrt{5}/3^{3/4}, -\sqrt{5}/3^{1/4}\right), \\ P_3 = \left(0,0,0,-2\sqrt{5}/3^{1/4}\right), P_4 = \left(-3^{-1/4}10^{-1/2}, -\sqrt{5/2}/3^{3/4}, -\sqrt{5}/3^{3/4}, -\sqrt{5}/3^{1/4}\right), \\ P_5 = \left(0,0,-3^{1/4}\sqrt{5}, -3^{1/4}\sqrt{5}\right), P_6 = (0.90, 2.74, -0.98, -1.70). \end{aligned} \tag{A.1}$$

The 4-simplex with points (12345) has the same 4-simplex geometry as in [40, 41]. We choose P_6 in (A.1) so that we have the length symmetry $l_{12} = l_{13} = l_{15} = l_{23} = l_{25} = l_{35} \approx 3.40$, $l_{14} = l_{24} = l_{34} = l_{45} \approx 2.07$, $l_{16} = l_{36} = l_{56} \approx 3.25$, $l_{26} \approx 5.44$ and $l_{46} \approx 3.24$.

All tetrahedra and triangles are space-like. The tetrahedron 4-d normal vectors N_a are determined by the triple product of three segment-vectors $l_1^\mu, l_2^\mu, l_3^\mu$ (the segment-vectors are given by $P_i^\mu - P_j^\mu$) along three line-segments labeled by $1,2,3$ adjacent to a common point

$$(N_a)_\mu = \frac{\epsilon_{\mu\nu\rho\sigma} l_{a1}^\nu l_{a2}^\rho l_{a3}^\sigma}{\|\epsilon_{\mu\nu\rho\sigma} l_{a1}^\nu l_{a2}^\rho l_{a3}^\sigma\|}, \tag{A.2}$$

where the norms $\|\cdot\|$ is given by the Minkowski metric $\eta = \mathrm{diag}(-,+,+,+)$, and $\epsilon_{\mu\nu\rho\sigma}$ follows the convention $\epsilon_{0123} = 1$. We list below the 4-d normals $(N_a)_\mu$ of the tetrahedra in each 4-simplex:

- The first 4-simplex with points 12345:

$$N_1 = (1.07, -0.12, -0.17, -0.30)\,,\ N_2 = (1.07, -0.12, -0.17, 0.30)\,,$$
$$N_3 = (1.07, -0.12, 0.35, 0)\,,\ N_4 = (1.07, 0.37, 0, 0)\,,\ N_5 = (-1, 0, 0, 0)\,. \tag{A.3}$$

- The second 4-simplex with points 12456:

$$N_6 = (1, 0, 0, 0)\,,\ N_7 = (-1.15, -0.19, -0.26, 0.46)\,,\ N_8 = (1.06, 0.35, 0, 0)\,,$$
$$N_9 = (-1.15, -0.19, 0.53, 0)\,,\ N_{10} = (-1.15, -0.19, -0.26, -0.46)\,. \tag{A.4}$$

- The third 4-simplex with points 13456:

$$N_{11} = (-1, 0.02, 0, 0)\,,\ N_{12} = (-1, 0, 0, 0)\,,\ N_{13} = (1, -0.02, -0.01, 0.01)\,,$$
$$N_{14} = (1, -0.02, 0.01, 0)\,,\ N_{15} = (1, -0.02, -0.01, -0.01)\,. \tag{A.5}$$

The triangles within a 4-simplex are classified into two categories [13]: The triangle corresponds to the *thin wedge* if the inner product of normals is positive; The triangle corresponds to *thick wedge* if the inner product of normals is negative. The dihedral angle $\theta_{a,b}$ are determined by:

$$\begin{aligned} &\text{thin wedge:} && N_a \cdot N_b \ = \cosh\theta_{a,b}, \\ &\text{thick wedge:} && N_a \cdot N_b \ = -\cosh\theta_{a,b}. \end{aligned} \tag{A.6}$$

where the inner product is defined by η. Then we check the deficit angle δ_h associated to the shared triangle h

$$0 = \delta_h = \theta_{4,5} + \theta_{6,8} + \theta_{11,12} \approx 0.36 - 0.34 - 0.02, \tag{A.7}$$

which implies the Regge geometry is flat.

To determine the 3-d normals of triangles, we proceed with a similar method as in [41]. To transform all 4-d normals to $t^\mu = (1, 0, 0, 0)$, we use the following pure boost $\Lambda_a \in O(1, 3)$:

$$(\Lambda_a)^\nu{}_\rho = \sigma\eta^\nu_\rho + \frac{\sigma}{1 - \sigma N_a \cdot t}\Big(N_a^\nu N_{a\rho} + t^\nu t_\rho + \sigma N_a^\nu t_\rho - (1 - 2\sigma N_a \cdot t)\sigma t^\nu N_{a\rho}\Big), \tag{A.8}$$

where $\sigma = 1$ for $N_{a0} > 0$ or $\sigma = -1$ for $N_{a0} < 0$. Then, the 3-d normals $\vec{\mathfrak{n}}_{a,b}$ can be expressed by Λ_a and 4-d normals:

$$\mathfrak{n}_{a,b} := (0, \vec{\mathfrak{n}}_{a,b}) = (\Lambda_a)^\nu{}_\rho \frac{N_b^\rho + N_a^\rho\,(N_b \cdot N_a)}{\sqrt{(N_b \cdot N_a)^2 - 1}}. \tag{A.9}$$

Here, $\vec{\mathfrak{n}}_{a,b}$ are the outward normals of the triangles in the tetrahedron a, then the inward normals are $-\vec{\mathfrak{n}}_{a,b}$. We associate $\vec{n}_{a,b} = \vec{\mathfrak{n}}_{a,b}$ (or $-\vec{\mathfrak{n}}_{a,b}$) to a strand oriented outward from (or inward to) the box labelled by g_a. The data of $\vec{\mathfrak{n}}_{a,b}$ can be found in the Mathematica notebook [30].

The spinors ξ_{eb} in Eq.(2.3) relate to $\vec{n}_{a,b}$ by $\vec{n}_{a,b} = \langle \xi_{a,b}, \vec{\sigma}\xi_{a,b}\rangle$. We use the following rule to convert a unit 3-vector to a normalized spinor (by fixing the phase convention):

$$\vec{n}_{a,b} = (x, y, z) \quad \to \quad \xi_{a,b} = \frac{1}{\sqrt{2}}\left(\sqrt{1+z},\ \frac{x+iy}{\sqrt{1+z}}\right). \tag{A.10}$$

The data for $j_{a,b}, \xi_{a,b}$ are listed in Tables 1, 2, 3. In these tables, $j_{a,b}, \xi_{a,b}$ for the internal face are labeled in the bold text, and the others are the boundary data. We denote the boundary data in these tables by $\mathring{r} = (\mathring{j}_b, \mathring{\xi}_{eb})$.

Table 1. Geometry data $\mathring{j}_{a,b}, \mathring{\xi}_{a,b}$ for 1st 4-simplex with points 12345

$\mathring{\xi}_{a,b}$ a \ b	1	2	3	4	5
1	⟍	(1.,0.01 + 0.01i)	(0.87,0.01+0.49i)	(0.87,0.46+0.17i)	(0.3, -0.55-0.78i)
2	(1,-0.01,-0.01i)	⟍	(0.49,0.02+0.87i)	(0.49,0.82+0.31i)	(0.95,-0.17-0.25i)
3	(0.86,-0.01+0.51i)	(0.51,-0.02+0.86i)	⟍	(0.71,0.56-0.43i)	(0.71,-0.24+0.67i)
4	(0.86,0.48+0.16i)	(0.51,0.82+0.27i)	(0.71,0.59-0.39i)	⟍	**(0.71, 0.71)**
5	(0.3,-0.55-0.78i)	(0.95,-0.17-0.25i)	(0.71,-0.24+0.67i)	**(0.71, 0.71)**	⟍

$\mathring{j}_{a,b}$ a \ b	1	2	3	4	5
1	⟍	2	2	2	5
2	⟍	⟍	2	2	5
3	⟍	⟍	⟍	2	5
4	⟍	⟍	⟍	⟍	**5**

Table 2. Geometry data $\mathring{j}_{a,b}, \mathring{\xi}_{a,b}$ for 2nd 4-simplex with points 12456

$\mathring{\xi}_{a,b}$ a \ b	6	7	8	9	10
6	⟍	(0.95,-0.17-0.25i)	**(0.71, 0.71)**	(0.71,-0.24+0.67i)	(0.3,-0.55-0.78i)
7	(0.95,-0.17-0.25i)	⟍	(0.29,-0.47+0.83i)	(0.88,-0.02-0.48i)	(1,-0.02-0.03i)
8	**(0.71, 0.71)**	(0.31,-0.57+0.76i)	⟍	(0.71,0.25+0.66i)	(0.31,0.57-0.76i)
9	(0.71,-0.24+0.67i)	(0.85,0.02-0.52i)	(0.71,0.19+0.68i)	⟍	(0.85,-0.02+0.52i)
10	(0.3,-0.55-0.78i)	(1,0.02+0.03i)	(0.29,0.47-0.83i)	(0.88,0.02+0.48i)	⟍

$j_{a,b}$ a \ b	6	7	8	9	10
6	⟍	5	**5**	5	5
7	⟍	⟍	4.71	5.19	5.19
8	⟍	⟍	⟍	4.71	4.71
9	⟍	⟍	⟍	⟍	5.19

Table 3. Geometry data $\mathring{j}_{a,b}, \mathring{\xi}_{a,b}$ for 3rd 4-simplex with points 13456

$\mathring{\xi}_{a,b}$ a \ b	11	12	13	14	15
11	⟍	**(0.71, 0.71)**	(0.31,-0.57+0.76i)	(0.71,0.25+0.66i)	(0.31,0.57-0.76i)
12	**(0.71, 0.71)**	⟍	(0.51,0.82+0.27i)	(0.71,0.59-0.39i)	(0.86,0.48+0.16i)
13	(0.31,-0.57+0.76i)	(0.51,0.82+0.27i)	⟍	(0.5,0.87i)	(0,0.95+0.31i)
14	(0.71,0.25+0.66i)	(0.71,0.59-0.39i)	(0.5,0.87i)	⟍	(0.5,-0.87i)
15	(0.31,0.57-0.76i)	(0.86,0.48+0.16i)	(0,-0.95-0.31i)	(0.5,-0.87i)	⟍

$j_{a,b}$ a \ b	11	12	13	14	15
11	⟍	**5**	4.71	⟍	⟍
12	⟍	⟍	2	2	2
13	⟍	⟍	⟍	3.18	3.18
14	4.71	⟍	⟍	⟍	3.18
15	4.71	⟍	⟍	⟍	⟍

Once the flat geometry data $\mathring{\xi}_{a,b}$ and $\mathring{j}_{a,b}$ are constructed, we are ready to obtain the real critical points $\mathring{x} = (\mathring{j}_h, \mathring{g}_a, \mathring{\mathbf{z}}_{a,b})$ by solving the critical point equations Eq.(3.1) and (3.2). Here $\mathring{j}_h = \mathring{j}_{4,5} = \mathring{j}_{6,8} = \mathring{j}_{11,12} = 5$ is the same as the area of h.

A.2 The real critical point

The solution of the critical point equations relates to the Lorentzian Regge geometry, as described in [13, 14]. $\mathring{g}_a$ relates to the Lorentzian transformation acting on each tetrahedron and gluing them together to form the Δ_3 triangulation. The general form of $\mathring{g}_a$ can be expressed by:

$$\mathring{g}_a = \exp\left(\theta_{\text{ref},\,a}\vec{n}_{\text{ref},\,a}\cdot\frac{\vec{\sigma}}{2}\right), \tag{A.11}$$

where $\theta_{\text{ref},\,a}$ is the dihedral angle which is defined in Eq. (A.6), $\vec{\sigma}$ are the Pauli matrices, and $\text{ref} = 5, 6, 12$ are the reference tetrahedra, whose 4-d normals equal $\pm t$. The data for 3-d normals $\vec{n}_{\text{ref},\,a}$ can be found in Mathematica notebook [30]. On Δ_3 triangulation, we fix g_a to be constant $\text{SL}(2,\mathbb{C})$ matrices for $a = 1, 10, 15$ [3], and the group elements g_a for the bulk tetrahedra $a = 5, 8, 12$ are fixed to be the upper triangular matrix.

By Eq.(A.11) and the gauge fixing for g_{ve}, $\mathbf{z}_{vf}$, we obtain the numerical results of the real critical points $(\mathring{j}_h, \mathring{g}_a, \mathring{\mathbf{z}}_{a,b})$ corresponding to the flat geometry and all $s_v = +1$. $j_h = 5$ as the area of the internal triangle. The numerical data of $\mathring{g}_a$, $\mathring{\mathbf{z}}_{a,b}$ are shown in Table 4, 5 and 6.

[3] The choice of $a = 1, 10, 15$ for the $\text{SL}(2,\mathbb{C})$ gauge fixing is different from the $\text{ref} = 5, 6, 12$, because we would like to apply the $\text{SL}(2,\mathbb{C})$ and $\text{SU}(2)$ gauge fixings to different sets of g_a's.

Table 4. The real critical point $\mathring{g}_a$, $\mathring{\mathbf{z}}_{a,b}$ for the 1st 4-simplex with points 12345.

a	1	2	3
$\mathring{g}_a$	$\begin{pmatrix} 0.87 & -0.06+0.09i \\ -0.06-0.09i & 1.16 \end{pmatrix}$	$\begin{pmatrix} 1.16 & -0.06+0.09i \\ -0.06-0.09i & 0.87 \end{pmatrix}$	$\begin{pmatrix} 1.02 & -0.06-0.17i \\ -0.06+0.17i & 1.02 \end{pmatrix}$
a	4	5	
$\mathring{g}_a$	$\begin{pmatrix} 1.03 & 0 \\ 0.36 & 0.97 \end{pmatrix}$	$\begin{pmatrix} 1 & 0 \\ 0 & 1 \end{pmatrix}$	

$\lvert\mathring{\mathbf{z}}_{a,b}\rvert$ a \ b	7	8	9	10
6	(1,-0.18 - 0.26i)	(1,1)	(1,0.42 + 0.22i)	(1,-0.33 + 0.94i)
7	\	(1,-1.94 + 1.26i)	(-0.1 - 0.43i)	(1,-0.08 - 0.12i)
8	\	\	(1,0.03 + 1.i)	(1,0.22 - 3.72i)
9	\	\	\	(1,-0.13 + 0.74i)

Table 5. The real critical point $\mathring{g}_a$, $\mathring{\mathbf{z}}_{a,b}$ for the 2nd 4-simplex with points 12456.

a	6	7	8
$\mathring{g}_a$	$\begin{pmatrix} 1 & 0 \\ 0 & 1 \end{pmatrix}$	$\begin{pmatrix} 0.82 & 0.09-0.13i \\ 0.09+0.13i & 1.26 \end{pmatrix}$	$\begin{pmatrix} 0.97 & 0.34 \\ 0 & 1.03 \end{pmatrix}$
a	9	10	
$\mathring{g}_a$	$\begin{pmatrix} 1.04 & 0.09+0.25i \\ 0.09-0.25i & 1.04 \end{pmatrix}$	$\begin{pmatrix} 1.26 & 0.09-0.13i \\ 0.09+0.13i & 0.82 \end{pmatrix}$	

$\lvert\mathring{\mathbf{z}}_{a,b}\rvert$ a \ b	7	8	9	10
6	(1,-0.18 - 0.26i)	(1,1)	(1,0.42 + 0.22i)	(1,-0.33 + 0.94i)
7	\	(1,-1.94 + 1.26i)	(-0.1 - 0.43i)	(1,-0.08 - 0.12i)
8	\	\	(1,0.03 + 1.i)	(1,0.22 - 3.72i)
9	\	\	\	(1,-0.13 + 0.74i)

Table 6. The real critical point $\mathring{g}_a$, $\mathring{\mathbf{z}}_{a,b}$ for the 3rd 4-simplex with points 13456.

a	11	12	13
$\mathring{g}_a$	$\begin{pmatrix} 1.04 & -0.02 \\ -0.36 & 0.97 \end{pmatrix}$	$\begin{pmatrix} 0.97 & -0.36 \\ 0 & 1.03 \end{pmatrix}$	$\begin{pmatrix} 1.02+0.001i & -0.19+0.003i \\ -0.19-0.003i & 1.01-0.001i \end{pmatrix}$
a	14	15	
$\mathring{g}_a$	$\begin{pmatrix} 1.012-0.001i & -0.19-0.006i \\ -0.19+0.006i & 1.02+0.001i \end{pmatrix}$	$\begin{pmatrix} 1.01+0.001i & -0.19+0.003i \\ -0.19-0.003i & 1.02-0.001i \end{pmatrix}$	

$\lvert\mathring{\mathbf{z}}_{a,b}\rvert$ a \ b	11	12	13	14	15
11	\	(1,1)	(1,0.1 + 3.73i)	\	\
12	\	\	(1,1.41 + 0.31i)	(1, 0.92 - 0.4i)	(1,0.68 + 0.15i)
13	\	\	\	(1,0.68 + 1.52i)	(1,5.35 + 0.08i)
14	(1,0.64 + 0.77i)	\	\	\	(1,0.67 - 1.5i)
15	(1,1.92 - 1.16i)	\	\	\	\

All the boundary data $\mathring{r} = (\mathring{j}_{a,b}, \mathring{\xi}_{a,b})$ and the data of the real critical point $(\mathring{j}_h, \mathring{g}_a, \mathring{\mathbf{z}}_{a,b})$ can be found in the Mathematica notebook in [30].

We focus on the Regge-like boundary data $r = \{j_b, \xi_{eb}\}$. The Regge-like boundary data determines the geometries of boundary tetrahedra that are glued with the shape-matching and orientation-matching conditions [16] to form the boundary Regge geometry on $\partial\Delta_3$. Then the resulting boundary segment-lengths uniquely determine the 4d Regge geometry $\mathbf{g}(r)$ on Δ_3. The above $\mathring{r} = (\mathring{j}_{a,b}, \mathring{\xi}_{a,b})$ is an example of the Regge-like boundary data, which determine the flat geometry $\mathbf{g}(\mathring{r})$ on Δ_3. Generic Regge-like boundary conditions r determines the curved geometries $\mathbf{g}(r)$.

A.3 Parametrization of variables

Given the Regge-like boundary condition r, we find the *pseudo-critical point* $(j_h^0, g_a^0, \mathbf{z}_{a,b}^0)$ inside the integration domain, where $(j_h^0, g_a^0, \mathbf{z}_{a,b}^0)$ only satisfies $\mathrm{Re}(S) = \partial_{g_{ve}} S = \partial_{\mathbf{z}_{vf}} S = 0$ but does not necessarily satisfy $\partial_{j_h} S = 4\pi i k_h$. The pseudo-critical point $(j_h^0, g_a^0, \mathbf{z}_{a,b}^0)$ is the critical point of the spinfoam amplitude with fixed j_h, j_b [14], and endows the Regge geometry $\mathbf{g}(r)$ and all $s_v = +1$ to Δ_3. It reduces to the real critical point $(\mathring{j}_h, \mathring{g}_a, \mathring{\mathbf{z}}_{a,b})$ when $r = \mathring{r}$. $(j_h^0, g_a^0, \mathbf{z}_{a,b}^0)$ is close to $(\mathring{j}_h, \mathring{g}_a, \mathring{\mathbf{z}}_{a,b})$ in the integration domain when r is close to $\mathring{r}$ (by the natural metrics on the integration domain and the space of r). The data of the pseudo-critical points are given in [30].

We consider a neighborhood enclose both $(j_h^0, g_a^0, \mathbf{z}_{a,b}^0)$ and $(\mathring{j}_h, \mathring{g}_a, \mathring{\mathbf{z}}_{a,b})$. We use the following real parametrizations of the integration variables, according to the gauge-fixing in A.2,

- As $a = 1, 10, 15$, $g_a = g_a^0$.
- As $a = 5, 8, 12$, g_a is gauge-fixed to be an upper triangular matrix (g_a^0 is upper triangular):

$$g_a = g_a^0 \begin{pmatrix} 1 + \frac{x_a^1}{\sqrt{2}} & \frac{x_a^2 + i y_a^2}{\sqrt{2}} \\ 0 & \mu_a \end{pmatrix}, \tag{A.12}$$

  here, μ_a is determined by $\det(g_a) = 1$.

- As $a = 2, 3, 4, 6, 7, 9, 11, 13, 14$, g_a is parameterized as:

$$g_a = g_a^0 \begin{pmatrix} 1 + \frac{x_a^1 + iy_a^1}{\sqrt{2}} & \frac{x_a^2 + iy_a^2}{\sqrt{2}} \\ \frac{x_a^3 + iy_a^3}{\sqrt{2}} & \mu_a \end{pmatrix} \tag{A.13}$$

- The spinors are parametrized by two real parameters:

$$\mathbf{z}_{a,b} = (1, \alpha_{a,b}^0 + x_{a,b} + iy_{a,b}). \tag{A.14}$$

  where $\alpha_{a,b}^0$ is the second component of $\mathbf{z}_{a,b}^0$.

- For the internal spin j_h, we parametrize it by one real parameter

$$j_h = j_h^0 + \mathfrak{j}, \quad \mathfrak{j} \in \mathbb{R} \tag{A.15}$$

$x \in \mathbb{R}^{124}$ are denoted by these 124 real variables $\mathfrak{j}, x_a^{1,2,3}, y_a^{1,2,3}$, and $x_{a,b}, y_{a,b}$. The parametrizations define the coordinate chart covering the neighborhood enclosing both $x_0 = (j_h^0, g_a^0, \mathbf{z}_{a,b}^0)$ and $\mathring{x} = (\mathring{j}_h, \mathring{g}_a, \mathring{\mathbf{z}}_{a,b})$. This neighborhood is large since the parametrizations are valid generically. The pseudo-critical point is $x_0 = (0, 0, ..., 0)$, which contains 124 zero components. The spinfoam action can be expressed as $S(r, x)$. The integrals in (2.10) (for $\mathcal{K} = \Delta_3$) can be expressed as

$$\int \mathrm{d}^N x \, \mu(x) \, e^{\lambda S(r,x)}, \tag{A.16}$$

where $N = 124$. Both $S(r, x)$ and $\mu(x)$ is analytic in the neighborhood of $\mathring{x}$. We only focus on the integral $k_h = 0$ in (2.10), since other $k_h \neq 0$ integrals has no real critical point by the boundary data $\mathring{r}$. $S(r, x)$ can be analytic continue to a holomorphic function $\mathcal{S}(r, z)$, $z \in \mathbb{C}^N$ in a complex neighborhood of $\mathring{x}$. Here the analytic continuation is obtained by simply extending $x \in \mathbb{R}^N$ to $z \in \mathbb{C}^N$. The formal discussion of the analytic continuation of the spinfoam action is given in [42].

A.4 Geometrical variations

To obtain the curved geometries, we fix the geometries of the 4-simplices 12345 and 13456, but change the geometry of 4-simplex 12356 by varying the length of l_{26} (the length of the line segment connecting point 2 and 6) from $5.44 + 9.2 \times 10^{-17}$ to $5.44 + 9.2 \times 10^{-5}$. For each given l_{26}, we repeat the steps in A.1 and A.2 to reconstruct the geometry and compute all the geometric quantities, such as the triangle areas, the 4-d normals of tetrahedra, the 3-d normals of triangles, $\xi_{a,b}$, the deficit angle, etc. Part of the data for the fluctuation $\delta l_{26} = l_{26} - \mathring{l}_{26}$ and the corresponding deficit angle δ_h are shown in Table 7. These new geometries $\mathbf{g}(r)$ are curved geometries because of non-zero deficit angles.

Table 7. Each cell of the table is the value of internal deficit angle δ_h with fluctuation $\delta l_{26} = l_{26} - \mathring{l}_{26}$.

δl_{26}	9.2×10^{-17}	8.3×10^{-15}	7.3×10^{-14}	6.4×10^{-13}	4.6×10^{-11}	8.3×10^{-10}	7.3×10^{-9}	4.6×10^{-6}	9.2×10^{-6}	9.2×10^{-5}
δ_h	2.0×10^{-16}	1.8×10^{-14}	1.6×10^{-13}	1.40×10^{-12}	1.00×10^{-10}	1.81×10^{-9}	1.61×10^{-8}	1.00×10^{-5}	$2. \times 10^{-5}$	0.0002

A.5 Numerical solving complex critical points and error estimate

The absolute error ε in the case of $\gamma = 0.1$, $n = 4$ for some deficit angles are shown in Table 8. The absolute errors are small and have the scales as $\varepsilon \approx 1.31\delta_h^5$ at $n = 4$.

Table 8. Deficit angles δ_h and corresponding absolute errors

δ_h	2×10^{-16}	1.8×10^{-14}	1.6×10^{-13}	1.4×10^{-12}	1.0×10^{-10}	1.8×10^{-9}	1.6×10^{-8}	1.6×10^{-5}	2×10^{-5}	0.0002
ε	4.3×10^{-79}	2.5×10^{-69}	1.4×10^{-64}	7.1×10^{-60}	1.3×10^{-50}	2.5×10^{-44}	1.4×10^{-39}	1.4×10^{-24}	4.2×10^{-24}	4.2×10^{-19}

A.6 Flipping orientations and numerical results

Given the boundary data $\mathring{r}$, Table 9 lists δ_h^s's at different orientations.

Table 9.

s	$+++$	$---$	$++-$	$--+$	$+--$	$-+-$	$-++$	$+-+$
δ_h^s	0	0	0.043	−0.043	0.72	−0.72	−0.68	0.68

As in A.4, we deform the boundary data $r = \mathring{r} + \delta r$ to obtain curved geometries. Both real critical points with all $s_v = +$ and all $s_v = -$ move smoothly away from the real plane and become complex critical points. We numerically compute the other complex critical point $Z'(r)$ with all $s_v = -$ by the same procedure as in A.1-A.5. We compute

$$\delta\mathcal{I}(r) = \mathcal{S}(r, Z(r)) - i\mathcal{I}_R[\mathbf{g}(r)], \quad \delta\mathcal{I}'(r) = \mathcal{S}(r, Z'(r)) + i\mathcal{I}_R[\mathbf{g}(r)] \tag{A.17}$$

for the sequences of r of curved geometries. $\delta\mathcal{I}$ and $\delta\mathcal{I}'$ associate to two continuous orientations $s_v = +$ and $s_v = -$ respectively. Part of the results are shown in Table 10 at $\gamma = 0.1$.

Table 10. $\delta\mathcal{I}(r)$ and $\delta\mathcal{I}'(r)$ at different deficit angles $|\delta_h^{s_v}|$.

$\lvert\delta_h^{s_v}\rvert$	$2.\times10^{-15}$	1.4×10^{-12}	1×10^{-10}	1.61×10^{-8}	2×10^{-4}
$\delta\mathcal{I}$	$-6.36\times10^{-34}-3.34\times10^{-35}$	$-3.12\times10^{-28}-1.63\times10^{-27}i$	$-1.59\times10^{-24}-8.34\times10^{-24}i$	$-4.07\times10^{-20}-2.13\times10^{-19}i$	$-6.30\times10^{-12}-3.32\times10^{-11}i$
$\delta\mathcal{I}'$	$-6.36\times10^{-34}+3.34\times10^{-35}$	$-3.12\times10^{-28}+1.63\times10^{-27}i$	$-1.59\times10^{-24}+8.34\times10^{-24}i$	$-4.07\times10^{-20}+2.13\times10^{-19}i$	$-6.30\times10^{-12}+3.32\times10^{-11}i$

The best-fit functions are

$$\delta\mathcal{I}(r) = a_2(\delta_h^+)^2 + a_3(\delta_h^+)^3 + a_4(\delta_h^+)^4 + O((\delta_h^+)^5), \tag{A.18}$$
$$\delta\mathcal{I}'(r) = a_2^*(\delta_h^-)^2 - a_3^*(\delta_h^-)^3 + a_4^*(\delta_h^-)^4 + O((\delta_h^-)^5), \tag{A.19}$$

where $\delta_h^\pm \equiv \delta_h^{\pm\pm\pm}$. a_i^* is the complex conjugate of a_i. The best fit coefficient a_i and the corresponding fitting errors are

$$\begin{aligned} a_2 &= -0.00016_{\pm10^{-17}} - 0.00083_{\pm10^{-16}}i, \\ a_3 &= -0.0071_{\pm10^{-13}} - 0.011_{\pm10^{-12}}i, \\ a_4 &= -0.059_{\pm10^{-9}} + 0.070_{\pm10^{-8}}i. \end{aligned} \tag{A.20}$$

Fig 2(a) demonstrates the excellent agreement between the numerical data and the fitted polynomial function at $\gamma = 0.1$ and $\lambda = 10^{11}$.

Then, the asymptotic amplitude is obtained

$$A(\Delta_3) = \left(\frac{1}{\lambda}\right)^{60} \left[\mathscr{N}_r^+ e^{i\lambda\mathcal{I}_R[\mathbf{g}(r)]+\lambda\delta\mathcal{I}(r)} + \mathscr{N}_r^- e^{-i\lambda\mathcal{I}_R[\mathbf{g}(r)]+\lambda\delta\mathcal{I}'(r)}\right][1 + O(1/\lambda)]\,. \tag{A.21}$$

At $\gamma = 0.1, \delta_h^\pm \simeq \pm 2\times10^{-4}$, we have $\mathscr{N}_r^+/\mathscr{N}_r^- \simeq 0.001 + 0.005i, \mathcal{I}_R \simeq -0.22\gamma$, $\delta\mathcal{I}^+ \simeq -6.30\times10^{-12} - 3.32\times10^{-11}i$ and $\delta\mathcal{I}^- \simeq -6.30\times10^{-12} + 3.32\times10^{-11}i$.

B 1-5 Pachner move and $A(\sigma_{\text{1-5}})$

B.1 Flat geometry, boundary data, and real critial point

The triangulation $\sigma_{1\text{-}5}$ of the 1-5 pachner move is made by five 4-simplices. $\sigma_{1\text{-}5}$ is obtained by adding an point 6 inside a 4-simplex and connecting point 6 to the other 5 points of the 4-simplex by 5 line segments $(1,6),(2,6),\cdots,(5,6)$. The dual cable diagram of $\sigma_{1\text{-}5}$ is in Fig.4(b) [4] (see also [39]). $\sigma_{1\text{-}5}$ consists of 10 boundary triangles b (dual to black strands in Fig. 4(b)) and 10 internal triangles h (dual to colored loops in Fig. 4(b)). Here, we set the coordinates of P_1, P_2, P_3, P_4, P_5 the same as Eq.(A.1). The coordinate of the point 6 is

$$P_6 = (-0.068, -0.27, -0.50, -1.30)\,, \tag{B.1}$$

$P_1,\cdots,P_6$ determines a flat Regge geometry on $\sigma_{1\text{-}5}$. We obtain five Lorentzian 4-simplices, $S_{12346}, S_{12356}, S_{12456}, S_{13456}, S_{23456}$ with all tetrahedra and triangles space-like. The lengths of the internal line segments are $l_{16}\approx 2.01$, $l_{26}\approx 6.66$, $l_{36}\approx 4.72$, $l_{46}\approx 0.54$, $l_{56}\approx 6.19$. The 4-d normals are determined by Eq.(A.2). For convenience, we choose $(N_a)_\mu$ with $a = 2, 6, 13, 18, 23$ to be $(-1,0,0,0)$ as reference for each 4-simplex. Hence, the 4-d normals $(N_a)_\mu$ in each 4-simplex are given by:

- The first 4-simplex 12346:

$$N_1 = (1.02, -0.06, 0.17, 0),\quad N_2 = (-1,0,0,0),\quad N_3 = (-1.15, 0.07, -0.53, 0.19),$$
$$N_4 = (1.50, 0.98, -0.54, 0),\quad N_5 = (-1.04, 0.06, -0.28, -0.06).$$

- The second 4-simplex 12356:

$$N_6 = (-1,0,0,0),\quad N_7 = (1.02, -0.06, 0.17, 0),\quad N_8 = (1.00, -0.03, -0.04, 0.07),$$
$$N_9 = (1.03, 0.26, 0, 0),\quad N_{10} = (1.00, -0.02, -0.02, -0.04).$$

- The third 4-simplex 12456:

$$N_{11} = (1.0, -0.091, -0.13, 0.22),\quad N_{12} = (1.3, -0.11, 0.79, -0.28),\quad N_{13} = (-1,0,0,0),$$
$$N_{14} = (1.1, 0.50, 0.077, -0.13),\quad N_{15} = (-1.5, 0.14, 0.19, -1.1).$$

- The fourth 4-simplex 13456:

$$N_{16} = (1.0, 0.10, 0, 0),\quad N_{17} = (-1.2, -0.57, 0.30, 0),\quad N_{18} = (-1,0,0,0),$$
$$N_{19} = (-1.0, -0.19, -0.029, 0.049),\quad N_{20} = (-1.0, -0.14, -0.012, -0.020).$$

- The fifth 4-simplex 23456:

$$N_{21} = (1.0, -0.11, -0.15, -0.26),\quad N_{22} = (1.1, -0.11, 0.49, 0.10),\quad N_{23} = (-1,0,0,0),$$
$$N_{24} = (1.6, -0.16, -0.22, 1.3),\quad N_{25} = (1.1, 0.42, 0.037, 0.064).$$

[4] For convenience, the indexes of group variables in FIG. 4(b) are $a = 1, 2, \cdots, 25$, the corresponding tetrahedra e are labeled by the numbers in FIG.1(b) in the letter. The correspondence are: $g_1 \to e_{1,2,3,4}$, $g_2 \to e_{1,2,3,6}$, $g_3 \to e_{1,2,4,6}$, $g_4 \to e_{1,3,4,6}$, $g_5 \to e_{2,3,4,6}$, $g_6 \to e_{1,2,3,5}$, $g_7 \to e_{1,2,3,6}$, $g_8 \to e_{1,2,5,6}$, $g_9 \to e_{1,3,5,6}$, $g_{10} \to e_{2,3,5,6}$, $g_{11} \to e_{1,2,4,5}$, $g_{12} \to e_{1,2,4,6}$, $g_{13} \to e_{1,2,5,6}$, $g_{14} \to e_{1,4,5,6}$, $g_{15} \to e_{2,4,5,6}$, $g_{16} \to e_{1,3,4,5}$, $g_{17} \to e_{1,3,4,6}$, $g_{18} \to e_{1,3,5,6}$, $g_{19} \to e_{1,4,5,6}$, $g_{20} \to e_{3,4,5,6}$, $g_{21} \to e_{2,3,4,5}$, $g_{22} \to e_{2,3,4,6}$, $g_{23} \to e_{2,3,5,6}$, $g_{24} \to e_{2,4,5,6}$, $g_{25} \to e_{3,4,5,6}$.

Then we compute all dihedral angles $\theta_{a,b}$ in each 4-simplex. We check that all deficit angles δ_h, $h = 1, 2, \cdots, 10$ hinged by 10 internal triangles vanish,

$$0 = \delta_1 = \theta_{2,3} + \theta_{12,13} + \theta_{8,7} \approx -0.54 + 0.77 - 0.23, \qquad 0 = \delta_2 = \theta_{2,4} + \theta_{17,18} + \theta_{9,7} \approx 0.965 - 0.604 - 0.361,$$
$$0 = \delta_3 = \theta_{3,4} + \theta_{17,19} + \theta_{14,12} \approx 1.37 - 0.47 - 0.90, \qquad 0 = \delta_4 = \theta_{8,9} + \theta_{18,19} + \theta_{14,13} \approx -0.3 - 0.2 + 0.5,$$
$$0 = \delta_5 = \theta_{2,5} + \theta_{22,23} + \theta_{10,7} \approx -0.29 + 0.49 - 0.2, \qquad 0 = \delta_6 = \theta_{3,5} + \theta_{22,24} + \theta_{15,12} \approx -0.3 - 1.2 + 1.5,$$
$$0 = \delta_7 = \theta_{8,10} + \theta_{23,24} + \theta_{15,13} \approx -0.12 + 1.07 - 0.95, \qquad 0 = \delta_8 = \theta_{4,5} + \theta_{22,25} + \theta_{20,17} \approx 1.18 - 0.69 - 0.49,$$
$$0 = \delta_9 = \theta_{9,10} + \theta_{23,25} + \theta_{20,18} \approx -0.28 + 0.42 - 0.14, \qquad 0 = \delta_{10} = \theta_{14,15} + \theta_{24,25} + \theta_{20,19} \approx 1.26 - 1.17 - 0.09.$$

We adapt the similar steps as in Δ_3 with Eq.(A.8), (A.9) and (A.10) to compute the normalized spinors $\xi_{a,b}$. We compute areas $j_{a,b}$ in each 4-simplex:

$\xi_{a,b}$ a \ b	1	2	3	4	5
1	\	(0.71,-0.24+0.67i)	(0.86,0.01-0.51i)	(0.71,0.57-0.43i)	(0.51,0.02-0.86i)
2	(0.64,-0.26+0.72i)	\	(0.51+0.02i,-0.13+0.85i)	(0.66-0.04i,-0.64+0.40i)	(0.71+0.01i,-0.16+0.68i)
3	(0.97-0.03i,-0.03-0.25i)	(0.32,-0.14+0.94i)	\	(0.42-0.01i,-0.49+0.76i)	(-0.99-0.02i,-0.035-0.11i)
4	(0.56-0.02i,0.67-0.49i)	(0.82+0.05i,-0.51+0.24i)	(0.80+0.01i,-0.44+0.40i)	\	(0.54-0.02i,0.65-0.53i)
5	(0.69-0.05i,-0.01-0.72i)	(0.61,-0.19+0.77i)	(0.99-0.02i,-0.05-0.15i)	(0.81+0.09i,0.48-0.33i)	\

$j_{a,b}$ a \ b	1	2	3	4	5
1	\	5	2	2	2
2	\	\	1.7	0.96	2.8
3	\	\	\	0.29	0.60
4	\	\	\	\	0.76

$\xi_{a,b}$ a \ b	6	7	8	9	10
6	\	(0.71,-0.24 + 0.67i)	(0.30,0.55+0.78i)	(0.71,-0.71)	(0.95,0.17+0.25i)
7	(0.64,-0.26+0.72i)	\	(0.51+0.01i,-0.13+0.85i)	(0.66-0.04i,-0.64+0.40i)	(0.71+0.01i,-0.16+0.68i)
8	(0.33,0.55+0.77i)	(0.59+0.02i,-0.12+0.80i)	\	(0.62-0.02i,0.77+0.11i)	(0.14,0.57+0.81i)
9	(0.79,-0.61)	(0.78-0.04i,-0.53+0.32i)	(0.51-0.01i,0.85+0.12i)	\	(0.75,0.66-0.06i)
10	(0.96,0.17+0.24i)	(0.78,-0.15+0.61i)	(0.12,0.57+0.81i)	(0.65,-0.76-0.07i)	\

$j_{a,b}$ a \ b	6	7	8	9	10
6	\	\	5	5	5
7	5	\	\	\	\
8	\	1.7	\	1.6	3.2
9	\	0.96	\	\	2.7
10	\	2.8	\	\	\

$\xi_{a,b}$ a \ b	11	12	13	14	15
11	\	(0.87,-0.01-0.49i)	(0.30,0.55+0.78i)	(0.49,0.82+0.31i)	(0.015,0.58+0.82i)
12	(0.97-0.03i,-0.03-0.25i)	\	(0.32,-0.14+0.94i)	(0.42-0.01i,-0.48+0.76i)	(0.99-0.02i,-0.036-0.106i)
13	(0.33,0.55+0.77i)	(0.59+0.02i,-0.12+0.80i)	\	(0.62-0.02i,0.77+0.11i)	(0.14,0.57+0.81i)
14	(0.30-0.02i,0.91+0.30i)	(0.75-0.14i,-0.38+0.52i)	(0.41+0.01i,0.90+0.15i)	\	(0.09-0.024i,0.94+0.32i)
15	(0.14,0.57+0.81i)	(0.94-0.01i,-0.08-0.34i)	(0.21,0.56+0.80i)	(0.32-0.05i,0.86+0.39i)	\

$j_{a,b}$ a \ b	11	12	13	14	15
11	\	\	\	2	2
12	2	\	1.7	\	\
13	5	\	\	\	\
14	\	0.29	1.6	\	0.68
15	2	\	\	0.68	\

$\xi_{a,b}$ a \ b	16	17	18	19	20
16	\	(0.71,0.59-0.39i)	(0.71,-0.71)	(0.51,0.82+0.27i)	(0.51,-0.82-0.27i)
17	(0.56-0.02i,0.67-0.48i)	\	(0.82+0.06i,-0.51+0.23i)	(0.80+0.02i,-0.45+0.40i)	(0.54-0.01i,0.66-0.52i)
18	(0.79,-0.61)	(0.78-0.04i,-0.53+0.32i)	\	(0.51-0.01i,0.85+0.12i)	(0.75,-0.66-0.06i)
19	(0.30-0.02i,0.91+0.30i)	(0.75-0.15i,-0.38+0.53i)	(0.41+0.01i,0.90+0.15i)	\	(0.1-0.03i,0.95+0.32i)
20	(0.46-0.02i,0.85-0.27i)	(0.73-0.02i,0.53-0.43i)	(0.61,-0.79-0.06i)	(0.37+0.02i,0.88+0.30i)	\

$j_{a,b}$ a \ b	16	17	18	19	20
16	\	\	\	\	2
17	2	\	0.96	0.29	\
18	5	\	\	1.6	\
19	2	\	\	\	\
20	\	0.76	2.7	0.68	\

$\xi_{a,b}$ a \ b	21	22	23	24	25
21	\	(0.49,-0.02-0.87i)	(0.95,0.17+0.25i)	(0.015,-0.58-0.82i)	(0.49,-0.82-0.31i)
22	(0.69-0.05i,-0.01-0.72i)	\	(0.61,-0.18+0.77i)	(0.99-0.02i,-0.05-0.15i)	(0.81+0.09i,0.48-0.33i)
23	(0.96,0.17+0.24i)	(0.78,-0.15+0.61i)	\	(0.12,0.57+0.81i)	(0.65,-0.76-0.07i)
24	(0.141,0.57+0.81i)	(0.94-0.01i,-0.08-0.34i)	(0.21,0.56+0.80i)	\	(0.32-0.05i,0.86+0.39i)
25	(0.46-0.02i,0.84-0.27i)	(0.73-0.02i,0.53-0.43i)	(0.61,-0.79-0.06i)	(0.37+0.02i,0.88+0.30i)	\

$j_{a,b}$ a \ b	21	22	23	24	25
22	2	\	2.8	0.60	0.76
23	5	\	\	3.2	2.7
24	2	\	\	\	0.68
25	2	\	\	\	\

The boundary data $\mathring{r} = \{\mathring{j}_b, \mathring{\xi}_{eb}\}$ are given in the above tables. The real critical point $(\mathring{j}_h, \mathring{g}_a, \mathring{z}_{a,b})$ corresponding to the above flat Regge geometry is obtained by solving critical point equations Eqs. (3.1) and (3.2). To remove the gauge freedom, We choose g_a, $a = 1, 6, 11, 16, 21$, to be identity and g_a, $a = 2, 3, 8, 9, 14, 15, 17, 20, 22, 23$, to be upper triangular matrix. In each 4-simplex, we choose $a = 1, 6, 11, 16, 21$ as the references and use Eq.(A.11) to obtain critical points $\mathring{g}_a$. The resulting $\mathring{g}_a$ and $\mathring{z}_{a,b}$ are given below. The critical point in $\sigma_{1\text{-}5}$ endows the continuous orientation $s_v = -1$ to all 4-simplices.

a	1	2	3
$\mathring{g}_a$	$\begin{pmatrix} 1.02 & -0.06-0.17i \\ -0.06+0.17i & 1.02 \end{pmatrix}$	$\begin{pmatrix} 0.99 & -0.06-0.17i \\ 0 & 1.01 \end{pmatrix}$	$\begin{pmatrix} 0.83 & -0.12-0.61i \\ 0 & 1.20 \end{pmatrix}$
a	4	5	
$\mathring{g}_a$	$\begin{pmatrix} 0.99 & 0.55+0.29i \\ 0.25 & 1.14+0.074i \end{pmatrix}$	$\begin{pmatrix} 0.94 & -0.12-0.45i \\ 0 & 1.02 \end{pmatrix}$	

$\mathring{z}_{a,b}$ a \ b	2	3	4	5
1	(1,-0.33 + 0.94 i)	(1,0.08 - 0.69 i)	(0.68 - 0.73i)	(1,0.18 - 1.43 i)
2	\	(1,-0.14 + 1.50 i)	(1,-0.93 + 0.37i)	(1,-0.16 + 0.77i)
3	\	\	(1,-0.93 + 0.48i)	(1,0.078 - 0.58 i)
4	\	\	\	(1,0.64 - 0.88i)

a	6	7	8
$\mathring{g}_a$	$\begin{pmatrix} 1 & 0 \\ 0 & 1 \end{pmatrix}$	$\begin{pmatrix} 0.99 & -0.06-0.17i \\ 0 & 1.01 \end{pmatrix}$	$\begin{pmatrix} 1.03 & -0.03+0.045i \\ 0 & 0.96 \end{pmatrix}$
a	9	10	
$\mathring{g}_a$	$\begin{pmatrix} 0.98 & 0.25 \\ 0 & 1.02 \end{pmatrix}$	$\begin{pmatrix} 0.98 & -0.02+0.02i \\ 0 & 1.02 \end{pmatrix}$	

$\lvert\mathring{z}_{a,b}\rangle$ a \ b	6	7	8	9	10
6	\	\	(1,1.82 + 2.57i)	(1,-1)	(0.18 + 0.26i)
7	(1,-0.33 + 0.94i)	\	\	\	\
8	\	(1,-0.14+ 1.50i)	\	(1,1.36 + 0.27i)	(1,4.60 + 6.50i)
9	\	(1,-0.93 + 0.37i)	\	\	(1,-1.11 - 0.072i)
10	\	(1,-0.16 + 0.77i)	\	\	\

a	11	12	13
$\mathring{g}_a$	$\begin{pmatrix} 1.08 & -0.03+0.04i \\ -0.03-0.04i & 0.93 \end{pmatrix}$	$\begin{pmatrix} 0.77 & -0.08-0.62i \\ 0.02+0.04i & 1.32-0.02i \end{pmatrix}$	$\begin{pmatrix} 0.96 & 0 \\ 0.03+0.04i & 1.04 \end{pmatrix}$
a	14	15	
$\mathring{g}_a$	$\begin{pmatrix} 0.85 & 0.45-0.11i \\ 0 & 1.18 \end{pmatrix}$	$\begin{pmatrix} 1.52 & -0.14+0.2i \\ 0 & 0.66 \end{pmatrix}$	

$\lvert\mathring{z}_{a,b}\rangle$ a \ b	11	12	13	14	15
11	\	\	\	(1,1.77 + 0.80i)	(1,9.6 + 13.58i)
12	(1,0.03 - 0.62i)	\	(1,-0.23 + 1.31i)	\	\
13	(1,1.82 + 2.57i)	\	\	\	\
14	\	(1,-0.84 + 0.33i)	(1,1.21 + 0.14i)	\	(1,5.92 + 4.04i)
15	\	(1,0.027 - 0.53i)	(1,6.48 + 9.17i)	\	\

a	16	17	18
$\mathring{g}_a$	$\begin{pmatrix} 1.00 & -0.07 \\ -0.07 & 1.00 \end{pmatrix}$	$\begin{pmatrix} 0.96 & 0.27+0.28i \\ 0 & 1.04 \end{pmatrix}$	$\begin{pmatrix} 1.02 & 0 \\ -0.26 & 0.98 \end{pmatrix}$
a	19	20	
$\mathring{g}_a$	$\begin{pmatrix} 0.96+0.01i & 0.19-0.06i \\ -0.26-0.38i & 0.99 \end{pmatrix}$	$\begin{pmatrix} 1.01 & -0.12-0.01i \\ 0 & 0.99 \end{pmatrix}$	

$\lvert\mathring{z}_{a,b}\rangle$ a \ b	16	17	18	19	20
16	\	\	\	\	(1,-1.7 - 0.68i)
17	(1,0.87 - 0.48i)	\	(1,-0.82 + 0.58i)	(1,-0.76 + 0.75i)	\
18	(1,-1)	\	\	(1,1.21 + 0.14i)	\
19	(1,1.51 + 0.42i)	\	\	\	\
20	\	(1,0.88 - 0.59i)	(1,-1.20 - 0.13i)	(1,2.54 + 0.65i)	\

a	21	22	23
$\mathring{g}_a$	$\begin{pmatrix} 0.87 & -0.06+0.086i \\ -0.06-0.085i & 1.16 \end{pmatrix}$	$\begin{pmatrix} 0.97 & -0.13-0.45i \\ 0 & 1.03 \end{pmatrix}$	$\begin{pmatrix} 0.98 & -0.016+0.023i \\ 0 & 1.02 \end{pmatrix}$
a	24	25	
$\mathring{g}_a$	$\begin{pmatrix} 1.64 & -0.17+0.24i \\ -0.05-0.07i & 0.62 \end{pmatrix}$	$\begin{pmatrix} 1.04 & -0.14-0.01i \\ 0.26 & 0.99-0.003i \end{pmatrix}$	

$\lvert\mathring{z}_{a,b}\rangle$ a \ b	21	23	24	25
22	(1,0.18 - 1.43i)	(1,-0.15 + 0.78i)	(1,0.078 - 0.58i)	(1,0.64 - 0.88i)
23	(1,0.18 + 0.26i)	\	(1,4.6 + 6.5i)	(1,-1.11 - 0.072i)
24	(1,5.72 + 8.08i)	\	\	(1,4.58 + 3.90i)
25	(1,-1.41 - 0.31i)	\	\	\

B.2 Geometrical variations

Some data of the deformation $\delta l_{m6} = (\delta l_{16}, \delta l_{26}, \delta l_{36}, \delta l_{46}, \delta l_{56})$ and the corresponding deficit angles δ_h are shown in Tables 11 and 12,

Table 11. Deficit angles as $\delta l_{m6} = (3.0 \times 10^{-6}, 3.7 \times 10^{-6}, -3.1 \times 10^{-6}, -2.8 \times 10^{-6}, -3.6 \times 10^{-6})$

δ_1	δ_2	δ_3	δ_4	δ_5	δ_6	δ_7	δ_8	δ_9	δ_{10}	δ
6.1×10^{-5}	2.6×10^{-4}	1.1×10^{-4}	1.4×10^{-4}	4.6×10^{-5}	1.4×10^{-5}	1.8×10^{-5}	1.3×10^{-4}	1.1×10^{-4}	4.1×10^{-5}	1.2×10^{-4}

Table 12. Deficit angles as $\delta l_{m6} = (-3. \times 10^{-8}, 5.0 \times 10^{-8}, 3.4 \times 10^{-8}, 3.1 \times 10^{-8}, 4.0 \times 10^{-8})$

δ_1	δ_2	δ_3	δ_4	δ_5	δ_6	δ_7	δ_8	δ_9	δ_{10}	δ
1.5×10^{-6}	6.4×10^{-6}	2.8×10^{-6}	3.5×10^{-6}	1.1×10^{-6}	3.6×10^{-7}	4.5×10^{-7}	3.3×10^{-6}	2.8×10^{-6}	1.0×10^{-6}	2.9×10^{-6}

Here δ is the average of deficit angles $\delta = \sqrt{\frac{1}{10}\sum_{h=1}^{10}\delta_h^2}$.

B.3 Complex critical points and numerical results

The absolute errors in the case $\gamma = 1, n = 3$ for some averaged deficit angles are shown in the Table

δ	1.2×10^{-4}	1.2×10^{-5}	2.1×10^{-6}	6.5×10^{-7}	1.3×10^{-8}	1.2×10^{-10}	1.5×10^{-11}	1.4×10^{-12}
ε	4.0×10^{-15}	2.1×10^{-19}	2.0×10^{-22}	2.0×10^{-27}	2.3×10^{-31}	2.3×10^{-39}	5.0×10^{-43}	5.0×10^{-47}

Some numerical results of the difference $\delta\mathcal{I}(r_l) = \mathcal{S}(r_l, Z(r_l)) - S(r_l, x_0)$ at the complex critical points are shown in the Table

δ	1.2×10^{-4}	2.1×10^{-6}	3.8×10^{-8}	6.5×10^{-10}	6.5×10^{-12}
$\delta\mathcal{I}$	$-1.2 \times 10^{-12} + 4.5 \times 10^{-10} i$	$-3.8 \times 10^{-16} + 1.4 \times 10^{-13} i$	$-1.3 \times 10^{-19} + 4.7 \times 10^{-17} i$	$-3.8 \times 10^{-23} + 1.4 \times 10^{-20} i$	$-3.8 \times 10^{-27} + 1.4 \times 10^{-24} i$

The best-fit function is $\delta\mathcal{I} = -a_2(\gamma)\delta^2 + O(\delta^3)$, the best fit coefficient and the corresponding fitting errors at $\gamma = 1$ is:

$$a_2 = 8.88 \times 10^{-5}_{\pm 10^{-12}} - i0.033_{\pm 10^{-10}}. \tag{B.2}$$

We use FIG. 2(b) in the paper to demonstrate the excellent agreement between the numerical data and the best-fit function.

The Jacobian $\mathcal{J}_l$ in Eq. (6.6) reads:

$$\begin{aligned}
&\frac{l_{16}l_{26}l_{36}l_{46}l_{56}\left(l_{14}^2+l_{16}^2-l_{46}^2\right)\left(l_{15}^2+l_{16}^2-l_{56}^2\right)}{16\sqrt{-l_{12}^4+2\left(l_{16}^2+l_{26}^2\right)l_{12}^2-\left(l_{16}^2-l_{26}^2\right)^2}} \\
&\times\frac{\left\{\left[\left(l_{16}^2-l_{36}^2\right)\left(l_{26}^2-l_{36}^2\right)-l_{13}^2l_{23}^2\right]l_{12}^2+\left(l_{16}^2-l_{26}^2\right)\left[\left(l_{36}^2-l_{26}^2\right)l_{13}^2+l_{23}^2\left(l_{16}^2-l_{36}^2\right)\right]\right\}}{\sqrt{-l_{13}^4+2\left(l_{16}^2+l_{36}^2\right)l_{13}^2-\left(l_{16}^2-l_{36}^2\right)^2}\sqrt{-l_{23}^4+2\left(l_{26}^2+l_{36}^2\right)l_{23}^2-\left(l_{26}^2-l_{36}^2\right)^2}} \\
&\times\frac{1}{\sqrt{-l_{14}^4+2\left(l_{16}^2+l_{46}^2\right)l_{14}^2-\left(l_{16}^2-l_{46}^2\right)^2}\sqrt{-l_{15}^4+2\left(l_{16}^2+l_{56}^2\right)l_{15}^2-\left(l_{16}^2-l_{56}^2\right)^2}}.
\end{aligned}$$

References

[1] Thomas Thiemann. *Modern Canonical Quantum General Relativity.* Cambridge Monographs on Mathematical Physics. Cambridge University Press, 2007.

[2] Carlo Rovelli and Francesca Vidotto. *Covariant Loop Quantum Gravity: An Elementary Introduction to Quantum Gravity and Spinfoam Theory.* Cambridge Monographs on Mathematical Physics. Cambridge University Press, 11 2014.

[3] Alejandro Perez. The Spin Foam Approach to Quantum Gravity. *Living Rev.Rel.*, 16:3, 2013.

[4] Carlo Rovelli. Loop quantum gravity: the first twenty five years. *Class. Quant. Grav.*, 28:153002, 2011.

[5] Abhay Ashtekar and Jorge Pullin, editors. *Loop Quantum Gravity: The First 30 Years*, volume 4 of *100 Years of General Relativity.* World Scientific, 2017.

[6] Abhay Ashtekar and Eugenio Bianchi. A short review of loop quantum gravity. *Rept. Prog. Phys.*, 84(4):042001, 2021.

[7] Jonathan Engle, Roberto Pereira, and Carlo Rovelli. The Loop-quantum-gravity vertex-amplitude. *Phys. Rev. Lett.*, 99:161301, 2007.

[8] Jonathan Engle, Etera Livine, Roberto Pereira, and Carlo Rovelli. LQG vertex with finite Immirzi parameter. *Nucl. Phys. B*, 799:136–149, 2008.

[9] Carlo Rovelli. Graviton propagator from background-independent quantum gravity. *Phys. Rev. Lett.*, 97:151301, 2006.

[10] Etera R. Livine and Simone Speziale. A New spinfoam vertex for quantum gravity. *Phys. Rev. D*, 76:084028, 2007.

[11] Laurent Freidel and Kirill Krasnov. A New Spin Foam Model for 4d Gravity. *Class. Quant. Grav.*, 25:125018, 2008.

[12] Florian Conrady and Laurent Freidel. On the semiclassical limit of 4d spin foam models. *Phys. Rev.*, D78:104023, 2008.

[13] John W. Barrett, R. J. Dowdall, Winston J. Fairbairn, Frank Hellmann, and Roberto Pereira. Lorentzian spin foam amplitudes: Graphical calculus and asymptotics. *Class. Quant. Grav.*, 27:165009, 2010.

[14] Muxin Han and Mingyi Zhang. Asymptotics of Spinfoam Amplitude on Simplicial Manifold: Lorentzian Theory. *Class. Quant. Grav.*, 30:165012, 2013.

[15] Muxin Han and Thomas Krajewski. Path Integral Representation of Lorentzian Spinfoam Model, Asymptotics, and Simplicial Geometries. *Class. Quant. Grav.*, 31:015009, 2014.

[16] Wojciech Kaminski, Marcin Kisielowski, and Hanno Sahlmann. Asymptotic analysis of the EPRL model with timelike tetrahedra. *Class. Quant. Grav.*, 35(13):135012, 2018.

[17] Hongguang Liu and Muxin Han. Asymptotic analysis of spin foam amplitude with timelike triangles. *Phys. Rev. D*, 99(8):084040, 2019.

[18] José Diogo Simão and Sebastian Steinhaus. Asymptotic analysis of spin-foams with timelike faces in a new parametrization. *Phys. Rev. D*, 104(12):126001, 2021.

[19] Pietro Dona and Simone Speziale. Asymptotics of lowest unitary SL(2,C) invariants on graphs. *Phys. Rev. D*, 102(8):086016, 2020.

[20] J Engle, Wojciech Kaminski, and J Oliveira. Addendum to 'eprl/fk asymptotics and the flatness problem'. *Classical and Quantum Gravity*, 38(11):119401, 2021.

[21] Frank Hellmann and Wojciech Kaminski. Geometric asymptotics for spin foam lattice gauge gravity on arbitrary triangulations. *arXiv preprint arXiv:1210.5276*, 2012.

[22] Valentin Bonzom. Spin foam models for quantum gravity from lattice path integrals. *Phys. Rev. D*, 80:064028, 2009.

[23] Muxin Han. On Spinfoam Models in Large Spin Regime. *Class. Quant. Grav.*, 31:015004, 2014.

[24] Francesco Gozzini. A high-performance code for EPRL spin foam amplitudes. *Class. Quant. Grav.*, 38(22):225010, 2021.

[25] Jonathan Engle. The Plebanski sectors of the EPRL vertex. *Class. Quant. Grav.*, 28:225003, 2011. [Erratum: Class.Quant.Grav. 30, 049501 (2013)].

[26] Carlo Rovelli and Lee Smolin. Discreteness of area and volume in quantum gravity. *Nuclear Physics B*, 442(3):593–619, May 1995.

[27] Abhay Ashtekar and Jerzy Lewandowski. Quantum theory of geometry. 1: Area operators. *Class.Quant.Grav.*, 14:A55–A82, 1997.

[28] Anders Melin and Johannes Sjöstrand. Fourier integral operators with complex-valued phase functions. In Jacques Chazarain, editor, *Fourier Integral Operators and Partial Differential Equations*, pages 120–223, Berlin, Heidelberg, 1975. Springer Berlin Heidelberg.

[29] L. Hormander. *The Analysis of Linear Partial Differential Operators I*, chapter Chapter 7, page Theorem 7.7.5. Springer-Verlag Berlin, 1983.

[30] Dongxue Qu. https://github.com/dqu2017/Complex-critical-points-and-curved-geometries-in\-spinfoam-quantum-gravity, 2021.

[31] Pietro Donà, Francesco Gozzini, and Giorgio Sarno. Numerical analysis of spin foam dynamics and the flatness problem. *Phys. Rev. D*, 102(10):106003, 2020.

[32] Seth K. Asante, Bianca Dittrich, and Hal M. Haggard. Effective Spin Foam Models for Four-Dimensional Quantum Gravity. *Phys. Rev. Lett.*, 125(23):231301, 2020.

[33] Seth K. Asante, Bianca Dittrich, and Hal M. Haggard. Discrete gravity dynamics from effective spin foams. *Class. Quant. Grav.*, 38(14):145023, 2021.

[34] Seth K. Asante, Bianca Dittrich, and José Padua-Arguelles. Effective spin foam models for Lorentzian quantum gravity. *Class. Quant. Grav.*, 38(19):195002, 2021.

[35] Jonathan Engle and Carlo Rovelli. The accidental flatness constraint does not mean a wrong classical limit. *Class. Quant. Grav.*, 39(11):117001, 2022.

[36] The private communication with carlo rovelli.

[37] Benjamin Bahr and Sebastian Steinhaus. Numerical evidence for a phase transition in 4d spin foam quantum gravity. *Phys. Rev. Lett.*, 117(14):141302, 2016.

[38] Clement Delcamp and Bianca Dittrich. Towards a phase diagram for spin foams. *Class. Quant. Grav.*, 34(22):225006, 2017.

[39] Andrzej Banburski, Lin-Qing Chen, Laurent Freidel, and Jeff Hnybida. Pachner moves in a 4d Riemannian holomorphic Spin Foam model. *Phys. Rev. D*, 92(12):124014, 2015.

[40] Muxin Han, Zichang Huang, Hongguang Liu, and Dongxue Qu. Numerical computations of next-to-leading order corrections in spinfoam large-j asymptotics. *Phys. Rev. D*, 102(12):124010, 2020.

[41] Pietro Dona, Marco Fanizza, Giorgio Sarno, and Simone Speziale. Numerical study of the Lorentzian Engle-Pereira-Rovelli-Livine spin foam amplitude. *Phys. Rev.*, D100(10):106003, 2019.

[42] Muxin Han and Hongguang Liu. Analytic continuation of spinfoam models. *Phys. Rev. D*, 105(2):024012, 2022.